From the mantle source to the crustal sink: magmatic differentiation and sulfide saturation of the Paleoproterozoic komatiites of the Central Lapland Greenstone Belt, Finland

Ville J. Virtanen, Henri M. A. Höytiä, Giada Iacono-Marziano, Shenghong Yang, Marko Moilanen, Tuomo Törmänen

Contributions to Mineralogy and Petrology (2024) 179:73
https://doi.org/10.1007/s00410-024-02154-9

ORIGINAL PAPER

From the mantle source to the crustal sink: magmatic differentiation and sulfide saturation of the Paleoproterozoic komatiites of the Central Lapland Greenstone Belt, Finland

Ville J. Virtanen[1,2] · Henri M.A. Höytiä[2] · Giada Iacono-Marziano[1] · Shenghong Yang[3] · Marko Moilanen[3] · Tuomo Törmänen[4]

Received: 31 January 2024 / Accepted: 13 June 2024

Abstract

Paleoproterozoic (2.05 Ga) komatiites are widespread in the Central Lapland Greenstone Belt (CLGB), northern Finland. Close association with sulfur (S)-rich country rocks and spatiotemporal connection with the Cu-Ni(-PGE) deposits of Kevitsa and Sakatti make these komatiites interesting targets for sulfide deposit exploration. We provide whole-rock geochemical data from Sattasvaara komatiites and combine it with literature data to form a geochemical database for the CLGB komatiites. We construct a model for the komatiites from adiabatic melting of the mantle source to fractional crystallization at crustal conditions. Using MELTS, we calculate three parental melts (MgO = 20.6–25.7 wt%) in equilibrium with Fo_{92}, Fo_{93}, and Fo_{94} olivine for the CLGB komatiites. Based on REEBOX PRO simulations, these parental melts can form from a single mantle source by different pressures and degrees of melting when the potential temperature is 1575–1700 °C. We calculate ranges of S contents for the parental melts based on the different mantle melting conditions and degrees of melting. We use Magma Chamber Simulator to fractionally crystallize the parental melt at crustal conditions. These simulations reproduce the major element oxide, Ni, Cu, and S contents from our komatiite database. Simulated Ni contents in olivine are compatible with literature data from Kevitsa and Sakatti, hence providing a baseline to identify Ni-depleted olivine in CLGB komatiites and related intrusive rocks. We show that fractional crystallization of the komatiitic parental melt can form either Ni-rich or Cu-rich sulfide melt, depending on the initial Ni and S content of the parental melt.

Keywords Komatiite · Computational simulation · Mantle melting · Fractional crystallization · Sulfide saturation · Mineral exploration

Introduction

Komatiites represent high-degree melts that form as an anomalously hot portion of mantle undergoes (near) adiabatic decompression melting. Due to the requirement of high degree of melting, these magmas mostly formed during the Archean and Paleoproterozoic when the ambient mantle was relatively hotter compared to the modern mantle (e.g. Korenaga 2008). The degree of melting is typically thought to exceed 20%, which should be extensive enough to dissolve all sulfide from the mantle source (e.g., Arndt et al. 2005; Sossi et al. 2016; Yao et al. 2018; Waterton et al. 2021). After all sulfide is dissolved, further melting dilutes S content of the primary mantle melt and accordingly the degree of sulfide undersaturation should be highest in the

Communicated by Dante Canil.

✉ Ville J. Virtanen
ville.virtanen@cnrs-orleans.fr

[1] Institut des Sciences de la Terre d'Orléans, UMR 7327, Université d'Orléans, CNRS, BRGM, Orléans, OSUC F-45071, France

[2] Department of Geosciences and Geography, University of Helsinki, Helsinki, Finland

[3] Oulu Mining School, University of Oulu, Oulu, Finland

[4] Geological Survey of Finland, Rovaniemi, Finland

Published online: 26 June 2024

most magnesian komatiites. In the mantle, Cu and platinum group elements of the Pd-subgroup (PPGE: Pd, Pt, and Rh) are typically mainly compatible to sulfide, hence primary mantle melts related to komatiites effectively transport these elements from the mantle source to the crustal and surface levels. Partitioning of Ni during mantle melting is not as simple as it is compatible to olivine and sulfide in the mantle, but generally Ni content of the primary melt decreases with the degree of melting (Yao et al. 2018). The PGEs of the Ir-subgroup (IPGE: Ir, Or, and Ru) can be hosted in low-solubility metallic alloys, and partly in olivine in the case of Ru, hence their behavior in mantle melting is more complex compared to the PPGEs. Due to the high degree of mantle melting, komatiites tend to have high base metal and PPGE contents but require extensive olivine fractionation to reach sulfide saturation, which causes continuous depletion of Ni from the residual melt (Keays 1995; Arndt et al. 2005; Barnes and Lightfoot 2005). Nevertheless, some of the most Ni-rich sulfide deposits are related to komatiites (Barnes and Lightfoot 2005), due to early-stage sulfide saturation that is thought to result from assimilation of S-bearing country rocks (e.g. Lesher and Burnham 2001; Bekker et al. 2009). Physical properties such as high temperature and low viscosity make komatiites particularly capable to assimilate country rocks during their ascent and emplacement (e.g., Barnes et al. 2016).

The Central Lapland Greenstone Belt (CLGB) in the northern Finland, hosts a suite of Paleoproterozoic (ca. 2.05 Ga) komatiites that extend hundreds of kilometers through the Finnish Lapland and to Karasjok in the northern Norway. These so-called Savukoski Group komatiites show close spatial relationship with S-bearing black schists and sulfate evaporites, which make them interesting targets for base metal and PGE sulfide deposits. Indeed, the Kevitsa and Sakatti Cu-Ni-PGE sulfide deposits are spatiotemporally closely related to the komatiites and likely related to the same magmatic event (Brownscombe et al. 2015; Luolavirta et al. 2018a; Moilanen et al. 2021). Efforts have been made to estimate the mantle source and melting conditions of the CLGB komatiites (Hanski et al. 2001; Hanski and Kamenetsky 2013; Nicklas et al. 2019; Puchtel et al. 2020; Herzberg 2022) but the liquid line of descent that controls the sulfur content at sulfide saturation (SCSS) has not been constrained previously. Understanding of the SCSS and S content of the komatiitic parental melt is important because these variables control the onset of sulfide saturation in a fractionally crystallizing melt and quantifies how much external S assimilation is needed to reach early-stage sulfide saturation. Liquid and solid lines of descent for closed system fractional crystallization also provide chemical baselines against which the possible signs of assimilation in the natural data can be compared.

We present new whole-rock geochemical data from the Savukoski Group komatiites of CLGB from Sattasvaara area and combine it with literature data to form a comprehensive geochemical reference database for the CLGB komatiite suite. We use computational simulations to estimate the mantle melting conditions and the major element oxide, Ni, Cu, rare earth element (REE), as well as the S content of the primary mantle melt and the parental melt of the komatiites. Using the estimated parental melt composition, we conduct a fractional crystallization simulation to constrain a liquid line of descent and olivine composition (including Ni) that reproduce natural geochemical reference data from the CLGB komatiites with reasonable accuracy. We use the liquid line of descent to calculate the SCSS for fractionally crystallizing CLGB komatiites and to estimate the timing of sulfide saturation and composition of the sulfide phase. The constraints on liquid line of descent, sulfide saturation, and Ni content in olivine provide a useful reference, based on which the effects of assimilation-induced sulfide saturation can be compared to in following research or exploration campaigns.

Geological setting

The Paleoproterozoic Greenstone Belt association of Central Lapland, Pulju (western Lapland) and Karasjok (northern Norway) extends over several hundreds of kilometers in northern Fennoscandia and is among the largest greenstone belts in the world. These Fennoscandian greenstone belts can be lithostratigraphically correlated to ca. 2.5–1.9 Ga extensional regime (Papunen 1998; Hansen et al. 2023), when supracrustal rocks were deposited onto a rifting basin in the Archean Karelian Craton. The studied komatiites belong to CLGB, which spans the area between Kuusamo in eastern Finland and Kittilä in western Finnish Lapland (Fig. 1). The extension of the Archean Karelian Craton in CLGB initiated with deposition of the ca. 2.52–2.44 Ga Salla Group felsic-intermediate volcanic rocks, which were followed by deposition of ca. 2.44–2.38 Ga subaerial-subaqueous mafic and minor komatiitic magmatism of the Kuusamo Group (Luukas et al. 2017; Köykkä et al. 2019). The Salla Group volcanic rocks are cut by ca. 2.45–2.44 Ga widespread mafic layered intrusions, which have been interpreted to mark early migration of plume-related magmas to the lithosphere (Hanski and Huhma 2005). Following these magmatically active periods, an interval (ca. 2.38–2.22 Ga) characterized by increased sedimentation to a shallow ocean basin in syn- to early post-rift settings formed the Sodankylä Group rocks (Köykkä et al. 2019). Cross-cutting mafic sills constrain the minimum depositional age of the Sodankylä Group to ca. 2.2–2.15 Ga (Hanski and Huhma 2005). Graphitic-sulfidic

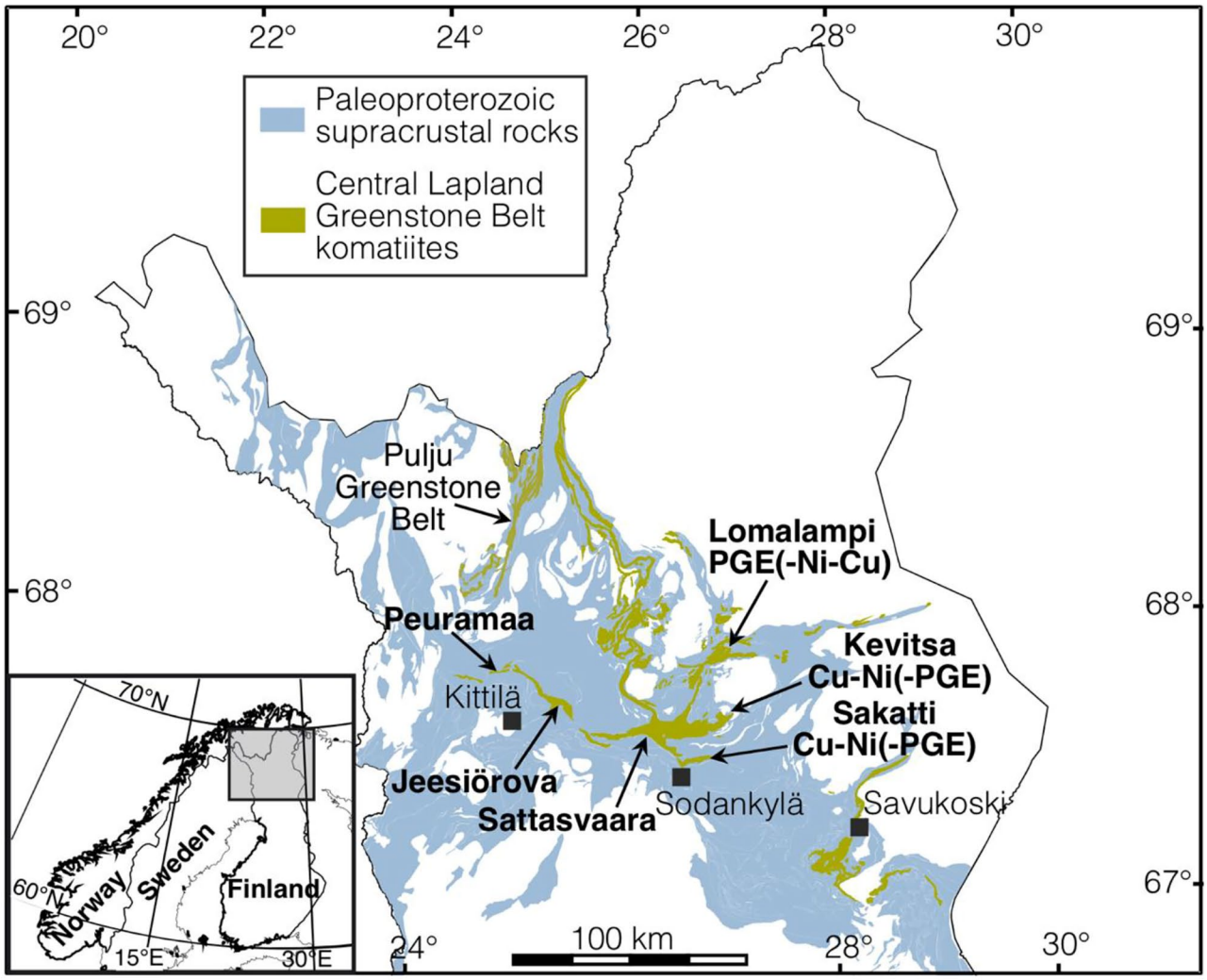

Fig. 1 Geological map showing the location of the Central Lapland Greenstone Belt and Paleoproterozoic supracrustal rocks in northern Finland (modified after Törmänen et al. 2015). The arrows with bold text indicate the approximate areas where the geochemical samples originate from

deep-sea sediments and sulfate evaporites of the ca. 2.15–2.05 Ga Savukoski Group overlie the Sodankylä Group rocks and indicate gradual deepening of the oceanic basin in a passive margin setting (Köykkä et al. 2019; Haverinen 2020). The main period of komatiitic-picritic magmatism in CLGB is spatiotemporally related to the deposition of the deep-sea sediments and accordingly the komatiitic-picritic rocks are included to the Savukoski Group.

The Savukoski Group komatiitic-picritic rocks are widespread along CLGB (Fig. 1) and have been suggested to implicate migration of a plume underneath the basin consisting of the Sodankylä and Savukoski Group sediments (Hanski and Huhma 2005; Luukas et al. 2017). Several isotopic systems (Sm-Nd, Re-Os, and Lu-Hf) have been used to date the komatiitic-picritic rocks of the Savukoski Group with the isochron ages spanning from 2046 Ma to 2072 Ma but being overlapping within uncertainty (Hanski et al. 2001: 2056 ± 25 Ma; Huhma et al. 2018: 2064 ± 38 Ma; Puchtel et al. 2020: 2049 ± 13 Ma, 2046 ± 22 Ma, 2072 ± 22 Ma). These komatiitic-picritic rocks are spatiotemporally and likely genetically connected with the ca. 2.05 Ga mafic-ultramafic intrusive magmatism, most notably the Kevitsa and Sakatti in CLGB (Mutanen and Huhma 2001; Luolavirta et al. 2018a; Moilanen et al. 2021) as well as Gállojávri in the northern Norway (Orvik et al. 2022). The komatiitic-picritic lavas were mostly deposited under water in phreatomagmatic eruptions, as characterized by their common textural features that include pyroclastic, amygdaloidal, and hyaloclastitic rocks as well as pillow lavas (Saverikko 1985; Barnes and Often 1990; Räsänen 2008). Quenched cooling breccias representative of the melt composition are common and minor spinifex-textured komatiites have been found (Räsänen 2008; Brownscombe et al. 2015). Cumulates of these komatiitic-picritic lavas are commonly found as

intrusive subvolcanic sills and channels, which also include more fractionated portions and marginal gabbroic rocks. As common for komatiites, olivine is the most abundant primary mineral with lesser clinopyroxene, and chromite is a typical minor phase (Hanski et al. 2001; Brownscombe et al. 2015; Puchtel et al. 2020). Orthopyroxene is present locally and plagioclase is present in the evolved rock types (Brownscombe et al. 2015). Stratigraphically, the komatiitic-picritic rocks are most commonly deposited onto the graphitic-sulfidic sediments and sulfate evaporites of the Savukoski Group, and furthermore all these lithologies are cut by ca. 2.05 Ga mafic-ultramafic intrusions. The stratigraphic position highlights Ni-Cu-PGE criticality of the komatiites, picrites, and coeval mafic-ultramafic intrusions, which is demonstrated by the Kevitsa and Sakatti Cu-Ni-PGE deposits (Santaguida et al. 2015; Brownscombe et al. 2015) as well as smaller PGE(-Ni-Cu) occurrences in Lomalampi (Törmänen et al. 2016), Pulju (Papunen 1998), and Karasjok (Orvik et al. 2022; Hansen et al. 2023).

Based on REE patterns and Al/Ti ratios, previous studies suggested that the komatiitic and picritic lavas were derived from different mantle sources (Hanski et al. 2001; Hanski and Kamenetsky 2013). This study focuses only on the petrogenesis of the komatiites because they are more common and widespread compared to the picrites, and, consequently, the availability of reference data is significantly better. The CLGB komatiites have distinct geochemical features that characterize their source and differentiation. The CLGB and Karasjok komatiites form a group of Fe-Ti-enriched komatiites ("Karasjok-type" in Arndt et al. 2008) with Al_2O_3/TiO_2 typically 10–15 (Hanski et al. 2001; Puchtel et al. 2020). The CLGB komatiites show typically "hump-shaped" REE patterns (chondrite-normalized La/Sm 0.2–0.5 and Gb/Yb 1.3–1.8), positive initial εNd and εHf values (ca. 2–5 and 10, respectively), and chondritic γOs values (Hanski et al. 2001; Hanski and Kamenetsky 2013; Gangopadhyay et al. 2006; Puchtel et al. 2020). The REE characteristics coupled with the εNd and εHf systematics indicate derivation from a depleted mantle source that originally formed hundreds of millions of years prior to the CLGB komatiite magmatism (Huhma et al. 2018; Puchtel et al. 2020). Estimated parental melt compositions range from komatiitic basalts with < 18 wt% MgO (Hanski et al. 2001; Törmänen et al. 2016) to high-MgO komatiite with 25 wt% MgO and mantle potential temperatures up to 1763 °C (Puchtel et al. 2020). Whole-rock MgO contents in the CLGB komatiites vary mostly between 10 and 30 wt% in lavas, and between 25 and 45 wt% in cumulates (Hanski et al. 2001; Brownscombe et al. 2015; Törmänen et al. 2016; Luolavirta et al. 2018a; Puchtel et al. 2020; Patten et al. 2023). Because some of the lavas contain < 18 wt% MgO they are not komatiites *sensu stricto*, however, in the framework of this study, we use the term komatiite to describe all rocks formed by fractionation of komatiitic parental melts (e.g., komatiitic basalts and gabbros).

The komatiitic-picritic magmatism terminated at the beginning of the subsequent collisional tectonic stage. This is marked by obduction of the juvenile oceanic crust of the Kittilä Group (ca. 2.15–1.92 Ga) and marine and alluvial sedimentation of the Kumpu Group (~ 1.92–1.88 Ga) to a foreland basin (Köykkä et al. 2019). The supracrustal sequence of CLGB was deformed and metamorphosed during Lapland-Kola (Daly et al. 2006), Lapland-Norrbotten, and Svecofennian (Lahtinen et al. 2005) orogenies, which account for the thrusting, folding and metamorphic overprint in greenschist to lower amphibolite facies that characterize the rocks in CLGB at present (Hölttä et al. 2017, Sayab et al. 2021). Although, the CLGB komatiites are commonly altered to serpentine, tremolite-actinolite, and chlorite, they have locally preserved pristine magmatic mineralogy including olivine, clinopyroxene, orthopyroxene, chromite, and plagioclase.

Materials and methods

Geological Survey of Finland collected 13 drill cores from two locations (Sattasköngäs and Sattasrimpi/Töyrylänmaa) in Sattasvaara area (Fig. 1), which represent differentiated portions of komatiitic magma, ranging from olivine-pyroxene cumulates to hyaloclastite lavas and gabbroic rocks (Räsänen 2008). From these drill cores, 49 samples including ultramafic (komatiitic) lavas and cumulates were analyzed for major element oxides and selected trace elements. The sample locations, coordinates (in the Finnish National Coordinate System format known as KKJ3), rock type descriptions, and compositional data are included in the Supplementary Material 1 (Table S1). The geochemical analyses were conducted by the Labtium Ltd using accredited methodology (SFS-EN ISO/IEC 17,025). To analyze major element oxides and selected trace elements (listed in Table S1), 15 to 20-cm-long split drill core samples were crushed with a jaw crusher (Mn-steel), pulverized with a tungsten carbide ball mill, and prepared as pressed powder pellets. The pellets were measured using a Philips PW1480 sequential wavelength dispersive X-ray fluorescence spectrometer (XRF). For the REE, Sc, Th, U, and Y the same jaw crusher aliquot was used but pulverization was done using a carbide steel vessel. The powder was dissolved first in HF-$HClO_4$ and then Li-metaborate-Na perborate after which the solution was measured using a Perkin-Elmer Sciex Elan 5000 inductively coupled plasma mass spectrometer (ICP-MS). The analytical precision of the XRF and ICP-MS measurements was monitored using well characterized

granite and peridotite as in-house quality control samples. Here we report the precision for the oxides and elements relevant for the simulations, whereas the full list is available in the Supplementary Materials (Table S1.1). The precision of XRF data is 2–4% for all major element oxides except P_2O_5, for which the precision is 16%. For Ni, the precision is 9%. The precision of the ICP-MS data is 12–22% for Gd and 17–27% for Y, and it increases with the concentration. More detailed descriptions of the XRF and ICP-MS methods including standardized sample preparation and measurement conditions can be found in Rasilainen et al. (2007). Samples for Au, Pt, and Pd measurements ($n = 27$) were prepared from 25 g powder aliquots using the standard Pb fire assay method and measured using inductively coupled plasma optical emission spectrometry.

In addition, we collected previously published whole-rock and melt inclusion data from CLGB ($n = 354$), including komatiitic lavas, dykes, and cumulates from Jeesiörova (Hanski et al. 2001; Hanski and Kamenetsky 2013), Kevitsa (Mutanen 1997; Luolavirta et al. 2018a; Puchtel et al. 2020), Sattasvaara (Saverikko 1985; Patten et al. 2023), and Lomalampi (Törmänen et al. 2016) areas (Fig. 1, Table S2). Most of these data (Mutanen 1997; Hanski et al. 2001; Törmänen et al. 2016; Luolavirta et al. 2018a; Patten et al. 2023) have been produced in the same laboratory and using the identical sample preparation techniques and measurement devices as the data original to this work. The major element oxide data of Saverikko (1985) was produced in the same laboratory using the same sample preparation method but with a Philips PW1400 spectrometer. The data of Saverikko (1985) shows no systematic deviations compared to the rest of the dataset. The whole-rock data of Puchtel et al. (2020) was acquired with similar methodology but in a different laboratory than the rest of the whole-rock data. The reported uncertainties for the data of Puchtel et al. (2020) are similar to the rest of the data and no systematic deviations are observable between the datasets. The komatiitic melt inclusions (Hanski and Kamenetsky 2013) were measured with electron microprobe analyzer (EMPA) and are compositionally similar to the whole-rock data. We also included Peuramaa samples to the reference database, although they are generally referred to as picrites that had possibly somewhat different mantle source compared to the coeval komatiites (Hanski et al. 2001; Hanski and Kamenetsky 2013). These data are similar to the komatiites with the exception of their generally higher TiO_2 contents. The number of whole-rock analyses vary slightly between elements and the number of measurements is indicated in the relevant figures and all data are available in the Supplementary Materials (Table S2).

The EMPA data for olivine ($n = 950$) is from Kevitsa (Yang et al. 2013; Luolavirta et al. 2018a; Nicklas et al. 2019; Puchtel et al. 2020) and Sakatti (Brownscombe et al. 2015; Höytiä unpublished) locations (Fig. 1, Table S3). Olivine grains associated with the Ni-PGE ore of Kevitsa were not included in the database as they have anomalously high Ni contents (up to > 14,000 ppm), which are ascribed to other processes than fractional crystallization and sulfide saturation (Yang et al. 2013). The unpublished analyses were conducted at the laboratory of the Geological Survey of Finland, Espoo, using a Cameca SX100 EMPA equipped with five wavelength-dispersive spectrometers. Focused beam, an accelerating voltage of 15 kV, and beam current of 60 nA were used. For Si, Mg, Fe, Cr, and Mn, peak and background measurement times were 10 s and 5 s, respectively. Peak/background measurement times for the rest of the elements were: Ca 60 s/15 s, Al 60 s/30 s, Ni 80 s/40 s, and K 40 s/20 s. The following standards were used: olivine (Si, Mg), diopside (Ca), almandine (Fe, Al), rhodonite (Mn), chromite (Cr), pentlandite (Ni), and sanidine (K). The analytical precision is 3% for major elements (> 10 wt%) and 5% for minor elements. The PAP computation method (Pouchou and Pichoir 1986) was used for the data treatment. The referenced olivine chemistry data can be found in the Supplementary Materials (Table S3).

Computational simulations

We conducted computational simulations to determine the parental melt compositions, conditions of mantle melting, and fractional crystallization at crustal conditions. The computational simulation strategy and the used software are summarized in Fig. 2 and the details are explained in the following subsections.

Constraining parental melt

Several chemical features of the parental melt of the CLGB komatiites have been estimated in previous studies (Hanski et al. 2001; Hanski and Kamenetsky 2013; Nicklas et al. 2019; Puchtel et al. 2020). The most recent and comprehensive parental melt composition estimations are based on a chilled margin of a komatiitic dyke that is spatially related to the Kevitsa intrusion (Nicklas et al. 2019; Puchtel et al. 2020; Table 1). The dyke contains well-preserved magmatic minerals and shows a clear textural and chemical evidence for olivine fractionation from the center with coarse-grained olivine cumulate to the fine-grained chilled margin with sparse olivine microphenocrysts (Nicklas et al. 2019; Puchtel et al. 2020). Oxygen fugacity (fO_2) of the parental melt was originally estimated to be $\Delta FMQ + 0.9$ (i.e., 0.9 log units higher than the fayalite-magnetite-quartz oxygen fugacity buffer) based on V partitioning between olivine and melt (Nicklas et al. 2019). However, the fO_2 was subsequently revised to $\Delta FMQ - 1.16$ with the positive error of

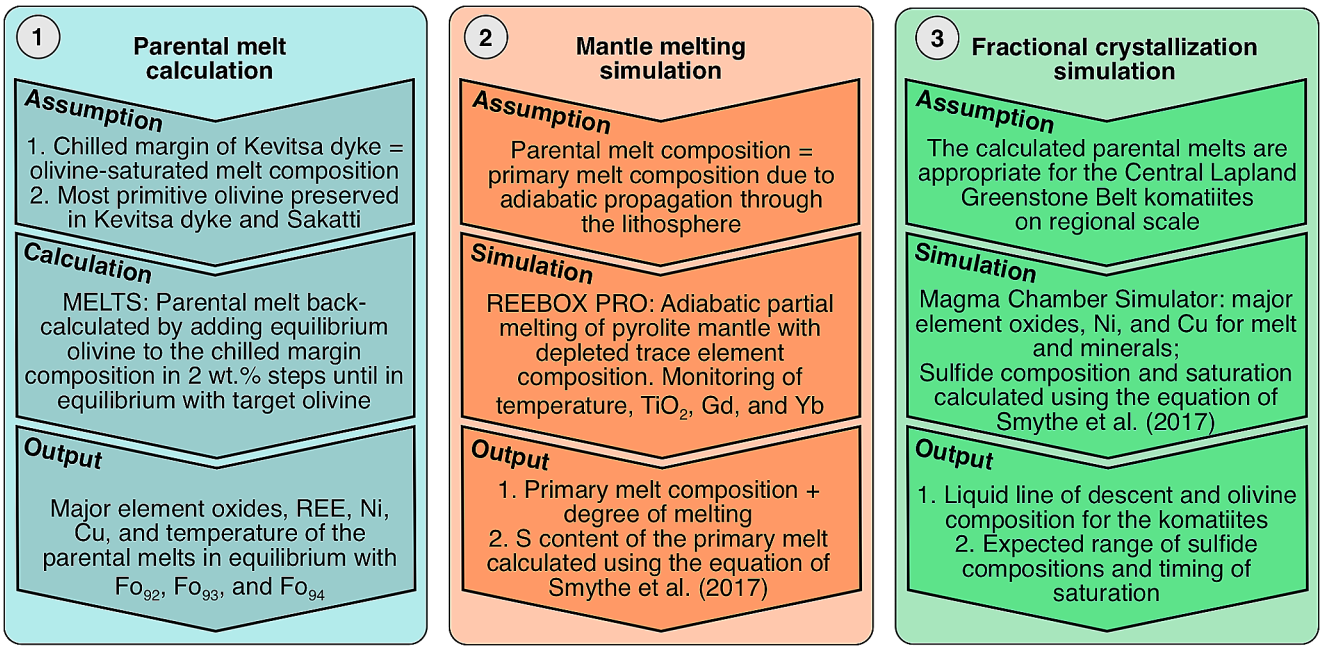

Fig. 2 A summary of the conducted calculations and simulations

0.21 and negative error of 0.19 (Nicklas et al. 2024). Puchtel et al. (2020) estimated some major element oxides and trace elements for the parental melt by incrementally adding equilibrium olivine to the chilled margin composition until reaching a melt composition in equilibrium with the most primitive olivine (Fo_{94}) in the dyke. However, none of the previous studies estimate all the major element oxides for the parental melt and hence the compositions cannot be used for our fractional crystallization simulations and SCSS calculations.

We estimate the parental melt composition from the chilled margin of the Kevitsa dyke following the previously used olivine addition method (Puchtel et al. 2020) with the following differences: (1) as the water content is not reported for the chilled margin, we approximate it to be ca. 0.05 wt% based on the H_2O/Ce of 200, which is in the range of values from several mantle sources (Kovalenko et al. 2007; Liu et al. 2017); (2) whereas Puchtel et al. (2020) calculated equilibrium olivine composition using the fO_2 range of ΔFMQ 0 to +0.9 (from Nicklas et al. 2019) and using the $K_{D_{ol-melt}}^{\Sigma Fe-Mg}$ formulation of Sossi and O'Neill (2016), we used rhyolite-MELTS (1.2.0) to calculate the composition of the equilibrium olivine within 5 °C from the liquidus and an fO_2 of ΔFMQ − 1, which is close to the value determined by Nicklas et al. (2024); (3) we calculate the melt in equilibrium with olivine having Fo_{92}, Fo_{93}, and Fo_{94}, to account for the possible heterogeneity in the komatiitic parental melts in the different parts of the CLGB. For example, the most primitive olivine with undepleted Ni content in the extensively sampled Sakatti olivine cumulates has Fo_{92} (Brownscombe et al. 2015), whereas magmatic olivine with $Fo_{93–94}$ has been only described from the Kevitsa dyke (Nicklas et al. 2019; Puchtel et al. 2020).

We simulated the addition of equilibrium olivine at a pressure of 25 MPa, which is relevant for subvolcanic dykes or intrusions at the depth of ca. 1 km and for submarine eruptions at the depth of ca. 2.5 km. To reach the parental melt compositions (Table 1) in equilibrium with Fo_{92}, Fo_{93}, and Fo_{94} olivine (PM^{Fo92}, PM^{Fo93}, PM^{Fo94}, respectively), we added olivine to the chilled margin composition in 2 wt% steps and without buffering fO_2, which leads to final range of fO_2 in the parental melts within uncertainty of the value determined from the Kevitsa dyke (Nicklas et al. 2024). The major element oxide composition and fO_2 of the parental melt are readily calculated by rhyolite-MELTS (1.2.0; Ghiorso and Gualda 2015). The contents of Ni, Cu, and REE were calculated based on trace element partition coefficients between olivine and melt. Several studies have reported temperature and composition dependent partitioning of Ni in olivine (e.g., Arndt 1977; Li et al. 2001; Matzen et al. 2013, 2017). We decided to use the formulation of Matzen et al. (2017) because it is based on thermodynamic properties of coexisting silicate melt and olivine defined using experimental data relevant to the simulated conditions. For Cu, we selected a static $K_{D_{ol-melt}}^{Cu}$ of 0.11 (Bédard 2005). For REE partitioning we used the parameterization of Bédard (2005) that depends on the MgO content of the melt. Partition coefficients for Pr and Tm are not reported in Bédard (2005) but were approximated as an average between their neighboring REEs. The major and trace element composition of the

Table 1 Composition of the chilled margin of the Kevitsa dyke as well as the parental melt and primary melt compositions for the Central Lapland Greenstone Belt komatiites. The parental and primary melt compositions were calculated from the chilled margin by olivine addition. We adjusted the fO_2 of the chilled margin to ΔFMQ − 1 to make the parental melts reach a final fO_2 close to the value (ca. ΔFMQ − 1.2) determined for the Kevitsa dyke (Nicklas et al. 2024)

Rock suite	Central Lapland Greenstone Belt komatiites (Kevitsa dyke)					
Source	Puchtel et al. (2020)		This study			
Rock/melt type	Chilled margin	Parental melt	Chilled margin	Parental melt = primary melt		
Method	Measured	Olivine addition	Adjusted fO_2[a]	Olivine addition[b]		
Liquidus T (°C)	-	1544	1375	1457	1498	1544
T_p[c]	-	1763	-	1575	1625	1700
ΔFMQ[d]	-	0 to + 0.9	-1	-1.14	-1.23	-1.34
Liquidus olivine	$Fo_{83.5–93.2}$[e]	Fo_{94}	$Fo_{89.7}$	$Fo_{92.1}$	$Fo_{93.1}$	$Fo_{93.9}$
SiO_2 (wt.%)	46.9	43.9	47.5	46.6	46.2	45.8
TiO_2	0.778	0.556	0.789	0.687	0.6	0.6
Al_2O_3	10.6	7.9	10.7	9.4	8.6	7.8
Fe_2O_3	13.0	12.4	1.2	1.1	1.0	0.9
Cr_2O_3	0.228	n.d.[f]	0.231	0.201	0.2	0.2
FeO	n.d.	n.d.	10.8	10.5	10.3	9.9
MnO	0.190	0.177	0.192	0.193	0.2	0.2
MgO	16.2	25.4	16.3	20.65	23.0	25.7
CaO	10.6	7.9	10.7	9.4	8.7	7.9
Na_2O	1.29	n.d.	1.31	1.14	1.1	1.0
K_2O	0.089	n.d.	0.090	0.079	0.1	0.1
P_2O_5	0.056	n.d.	0.057	0.049	0.05	0.04
H_2O	n.d.	n.d.	0.05	0.04	0.04	0.04
Total	99.93	98.20	100.00	100.00	100.00	100.00
Ni (ppm)	748	n.d.	748	816	882–1086	1033–1292
Cu	139	n.d.	139	122	115	105
La	0.687	0.253	0.687	0.599	0.553	0.502
Ce	2.40	1.30	2.40	2.09	1.93	1.75
Pr	0.526	0.34	0.526	0.458	0.423	0.384
Nd	3.62	2.48	3.62	3.15	2.91	2.64
Sm	1.66	1.18	1.66	1.45	1.34	1.21
Eu	0.677	n.d.	0.677	0.59	0.55	0.49
Gd	2.32	1.70	2.32	2.02	1.87	1.69
Tb	0.404	0.293	0.404	0.352	0.325	0.295
Dy	2.63	1.94	2.63	2.29	2.12	1.92
Ho	0.533	0.387	0.533	0.465	0.430	0.389
Er	1.44	1.06	1.44	1.26	1.16	1.05
Tm	0.196	0.144	0.196	0.171	0.158	0.144
Yb	1.26	0.926	1.26	1.10	1.02	0.92
Lu	0.179	0.133	0.179	0.156	0.144	0.131

[a]From Puchtel et al. (2020), Fe^{2+}/Fe^{3+} defined by MELTS to the reported fO_2, H_2O calculated based on $H_2O/Ce = 200$

[b]Equilibrium olivine added to the chilled margin. Compositions calculated using rhyolite-MELTS

[c]Mantle potential temperature

[d]Oxygen fugacity relative to the fayalite-magnetite-quartz buffer on logarithmic scale

[e]Range of measured compositions, not necessarily in equilibrium

[f]Not determined

parental melt calculated with the aforementioned method is listed in the Table 1.

Nickel content of the parental melt

Unlike incompatible Cu and REE, Ni is compatible in olivine and chromite, and hence estimating Ni content of the parental melt is sensitive to even small amount of autocrysts of these minerals in the chilled margin. Olivine microphenocrysts with Fo content up to 93.2 have been measured in the chilled margin of the Kevitsa dyke (Puchtel et al. 2020), which should be in equilibrium with Fo_{90} olivine (Table 1). This means that the chilled margin contains accumulated olivine, and possibly chromite, and does not strictly represent a quenched melt only. The accumulation of primitive high-Ni olivine means that the Ni content measured from the chilled margin sample is higher than that of the quenched melt. Because the amounts of accumulated olivine and chromite in the chilled margin sample are unknown, calculating the Ni content of the quenched melt is infeasible by removing these minerals. Instead, we use measured Ni contents in olivine that were analyzed from the Kevitsa dyke (Nicklas et al. 2019; Puchtel et al. 2020), to calculate the Ni content of the parental melt.

For the PM^{Fo92}, we selected the Ni content of 3340 ppm, which was measured from one olivine grain ($Fo_{92.5}$) in the Kevitsa dyke. Another suitable olivine grain ($Fo_{92.0}$) from the Kevitsa dyke has lower Ni content (3159 ppm) but we dismissed it because of the anomalously high Cr content (> 0.3 wt%). Using the Ni content of 3340 ppm in olivine and the $K_{D_{ol-melt}}^{Ni}$ of Matzen et al. (2017) gives parental melt with 816 ppm Ni (Table 1). Several olivine grains with $Fo_{93.1–93.3}$ (within analytical uncertainty compared to the Fo_{93} in parental melt) have been measured from the Kevitsa dyke (Nicklas et al. 2019). These grains contain a wide range of Ni content (3087–3802 ppm), which surpasses the analytical uncertainty of about 150–200 ppm (Nicklas et al. 2019). Instead of calculating an average value, we adopt the two extreme values for our olivine with Fo_{93}, which leads to PM^{Fo93} with Ni contents of 882–1086 ppm (Table 1). Olivine grains with $Fo_{93.7–94.1}$ and highly variable Ni contents (3142–3928 ppm) are also common in the Kevitsa dyke (Nicklas et al. 2019; Puchtel et al. 2020). Adopting the extreme values for our olivine with Fo_{94} constrains the Ni contents of the PM^{Fo94} to 1033–1292 ppm (Table 1).

Adiabatic mantle melting simulations

We conducted mantle melting simulations to estimate S content of the komatiitic parental melt. Sulfur content is not reported for the Kevitsa dyke (Puchtel et al. 2020) and hence it cannot be evaluated similarly to the other elements of the parental melt. In mantle-derived melts, the initial S content depends on the thermodynamic intensive variables (pressure, temperature, and major element oxide concentrations) and degree of melting in the mantle source. To simulate mantle melting we used pMELTS (version 5.6.1; Ghiorso et al. 2002) and REEBOX PRO (version 1.1; Brown and Lesher 2016). Whereas pMELTS is strictly based on thermodynamic properties of minerals and melt, REEBOX PRO determines mineral mode and degree of melting based on simple pressure dependent linear fitting to experimental data. The advantage of using pMELTS is that, unlike REEBOX PRO, it calculates the major element oxide contents of the evolving mantle melt, which is required to calculate how much S the melt can dissolve. However, simulations with pMELTS showed significant inconsistencies with the major element contents of melts from mantle melting experiments. The reason for this compositional difference arises most likely from the difficulties of pMELTS to accurately simulate garnet and olivine stabilities, as stated by Ghiorso et al. (2002). Hence, we consider that pMELTS simulations conducted with the current experimental parameterization cannot be used to make meaningful estimations for S dissolution in adiabatically formed mantle melts at the 3–4 GPa pressure range.

REEBOX PRO considers element mass balance only for Ti, K, and a selection of trace elements through partition coefficients, but it is parameterized to accurately replicate experimental data for mineral modes and melt production at 1–7 GPa pressure (for details and benchmarking, see Brown and Lesher 2016). Accordingly, REEBOX PRO provides estimates for P-T conditions and degree of melting in the mantle, while major element composition has to be estimated with an alternative method. We simulated mantle melting as adiabatic incremental batch melting [Standard (Langmuir) RMC in REEBOX PRO] of a pyrolite mineral mode, which is relevant for most upper and lower mantle regions (e.g., Green and Falloon 1998). In the chemical sense, incremental batch melting with melt extraction after each decompression step of 1 MPa approaches fractional melting, which is thought to be the dominant mode of mantle melting at the relevant pressure range of < 5–6 GPa (see discussion of Sossi et al. 2016). We simulated the pooling of the incrementally produced melt according to the column-accumulated melt mode of REEBOX PRO (Brown and Lesher 2016). For the mantle source, we selected the depleted mantle trace element compositions (Workmann and Hart 2005) and we conducted the simulations with the T_P between 1500 °C and 1700 °C with 25 °C intervals. We monitored the P-T conditions as well as Ti, Gd, and Yb contents of the produced primary mantle melt portion.

To approximate the major element oxide composition of the primary mantle melt, we propose it to be identical

to the parental melts calculated based on the Kevitsa dyke composition. This implies strictly adiabatic propagation through the lithosphere for the primary mantle melt – a process that has been previously proposed for the Gorgona komatiites (Herzberg et al. 2007). We evaluate the feasibility of adiabatic propagation by comparing the temperature as well as Ti, Gd, and Yb contents of the primary mantle melt produced by REEBOX PRO with the parental melts. We chose to monitor Gd and Yb for the degree of mantle melting because they are less affected by the earlier depletion of the mantle source (e.g., Hanski et al. 2001; Puchtel et al. 2020) compared to the more incompatible LREE. These elements are also present in higher concentrations in the natural rocks compared to many other REE, which makes the comparison more robust. To calculate temperature change during adiabatic rise of the primary mantle melt through the lithosphere, we used the experimentally defined P-T dependent komatiitic adiabat of 0.25 °C/MPa (Miller et al. 1991). We also tested if partially melting mantle is likely to produce major element oxide composition similar to the calculated parental melts. For this purpose, we combined the major element compositions of the parental melts with the calculated degrees of melting from REEBOX PRO and compared these with mantle melting experiments conducted with pyrolite (Walter 1998).

Fractional crystallization simulations

We conducted fractional crystallization simulations with the parental melt compositions (Table 1) using Magma Chamber Simulator (MCS; Bohrson et al. 2014, 2020), which calculates phase equilibrium using MELTS (Ghiorso and Sack 1995). We selected the rhyolite-MELTS (1.2.0; Ghiorso and Gualda 2015) for phase equilibrium and major element oxide calculations and conducted the simulations without buffering fO_2. We conducted the simulations isobarically at 25 MPa. With the PM^{Fo92}, we conducted an additional simulation with two isobaric stages at 1.2 GPa and 25 MPa. The two-stage simulation was conducted to test the effect of early orthopyroxene fractionation in the lower crust (ca. 44 km depth) on the Ni content in olivine at near-surface conditions. To examine liquid line of descent at a relevant range for sulfide saturation, we started the simulations at liquidus and decreased temperature in 5 °C steps until the temperature reached 1150°C. For Ni and Cu partitioning, we used the trace element extension of MCS (Heinonen et al. 2020). For olivine, we used the same partition coefficients as for the parental melt calculation (see above). For orthopyroxene, we used the $K^{Ni}_{D_{opx-melt}}$ and $K^{Cu}_{D_{opx-melt}}$ of Bédard (2007) that vary depending on the MgO content of the melt (only relevant for the 1.2 GPa stage of the two-stage simulation). For Cr-spinel, we used a $K^{Ni}_{D_{spl-melt}}$ of 2.77 and a $K^{Cu}_{D_{spl-melt}}$ of 0.66 based on measurement from chromites in low-Ti picrites (Barnes et al. 2023a). For clinopyroxene, we used the low-P (< 1 GPa) calibrations for terrestrial silicate systems of Bédard (2014) for $K^{Ni}_{D_{cpx-melt}}$ and $K^{Cu}_{D_{cpx-melt}}$, which depend on the MgO content of the melt. For Ni and Cu partitioning between plagioclase and melt, we used a $K^{Ni}_{D_{plg-melt}}$ of 0.06 and a $K^{Cu}_{D_{plg-melt}}$ of 0.17 (Bédard 2006).

Sulfide content at sulfide saturation calculation

Several formulations exist in the literature for calculating the SCSS (e.g., Fortin et al. 2015; Smythe et al. 2017; O'Neill 2021). Currently, only the formulations of Smythe et al. (2017) and O'Neill (2021) account for the effect of Ni and Cu on the SCSS, which can be on the order of 10^3 ppm (Smythe et al. 2017). The comparison presented by O'Neill (2021) shows that these two formulations are in good mutual agreement over most silicate melt compositions. The equation of O'Neill (2021) is intended mainly for basaltic and intermediate compositions, whereas the equation of Smythe et al. (2017) has been showed to accurately reproduce SCSS for experimental data ($n = 398$) ranging from 0.1 to $24*10^3$ MPa and 1150 to 2160 °C. Hence, we used the equation of Smythe et al. (2017), which considers the major element oxide composition of the melt, equilibrium sulfide composition, temperature, and pressure to calculate the SCSS. Sulfide composition is calculated based on the temperature and composition dependent element partitioning between sulfide and silicate melt defined by Kiseeva and Wood (2015). We calculated the SCSS for the primary mantle melt as well as for the parental melt undergoing fractional crystallization using the ideal solution model parameterization of the Smythe et al. (2017) equation. The mantle is somewhat heterogeneous in terms of S content but estimated values for depleted mid-ocean ridge basalt (MORB) mantle can be bracketed between 150 and 200 ppm (e.g., Lorand and Luquet 2016; Sun et al. 2020). Accordingly, to account for the uncertainty of the S content in the mantle source of the CLGB komatiites, we conducted simulations with the two extreme compositions.

Results

Primary mantle melt simulation

The REEBOX PRO simulations (Supplementary Material 2) produce primary melts that are similar with the target parental melts in terms of liquidus temperature, TiO_2, and Gd, when the analytical uncertainties of the Kevitsa dyke concentrations are considered. To simultaneously reproduce the TiO_2 and Gd contents as well as the liquidus temperatures at

25 MPa of the PM^{Fo92}, PM^{Fo93}, and PM^{Fo94}, the mantle T_P have to be close to 1575 °C, 1625 °C, and 1700 °C, respectively (Fig. 3a-b). The corresponding degrees of melting are 15–18% for PM^{Fo92}, 15–20% for PM^{Fo93}, and 20–22% for PM^{Fo94} (Fig. 3a-b). When the mantle T_P is 1575 °C, melting initiates at 5 GPa and the liquidus temperature of the PM^{Fo92} at 25 MPa, is reached if the partial melt detaches from the residual solids and rises adiabatically starting from 3.0 GPa (Fig. 3c). With the mantle T_P of 1625 °C, melting starts at 6.6 GPa and adiabatic rise of the partial melt needs to start at 4.0 GPa to reach the liquidus temperature of the PM^{Fo93} at 25 MPa (Fig. 3c). With the mantle T_P of 1700 °C, melting starts at 8.5 GPa and in order for the partial melt to reach the liquidus temperature of the PM^{Fo94} at 25 MPa, the detachment and adiabatic rise of the partial melt needs to start at 4.6 GPa (Fig. 3c). The P-T paths of the primary mantle melts, which form when the mantle T_P are 1575 °C and 1625 °C, reproduce the Gd/Yb of the PM^{Fo92} and PM^{Fo93}, respectively (Fig. 3d). However, the primary melt that forms with mantle T_P of 1700 °C, reaches the target Gd/Yb of the PM^{Fo94} when the degree of melting is 14–18% (Fig. 3d), which is lower than estimated based on the other monitored variables (Fig. 3a–c). The Gd/Yb of the Kevitsa dyke is similar to the average and median Gd/Yb of the CLGB

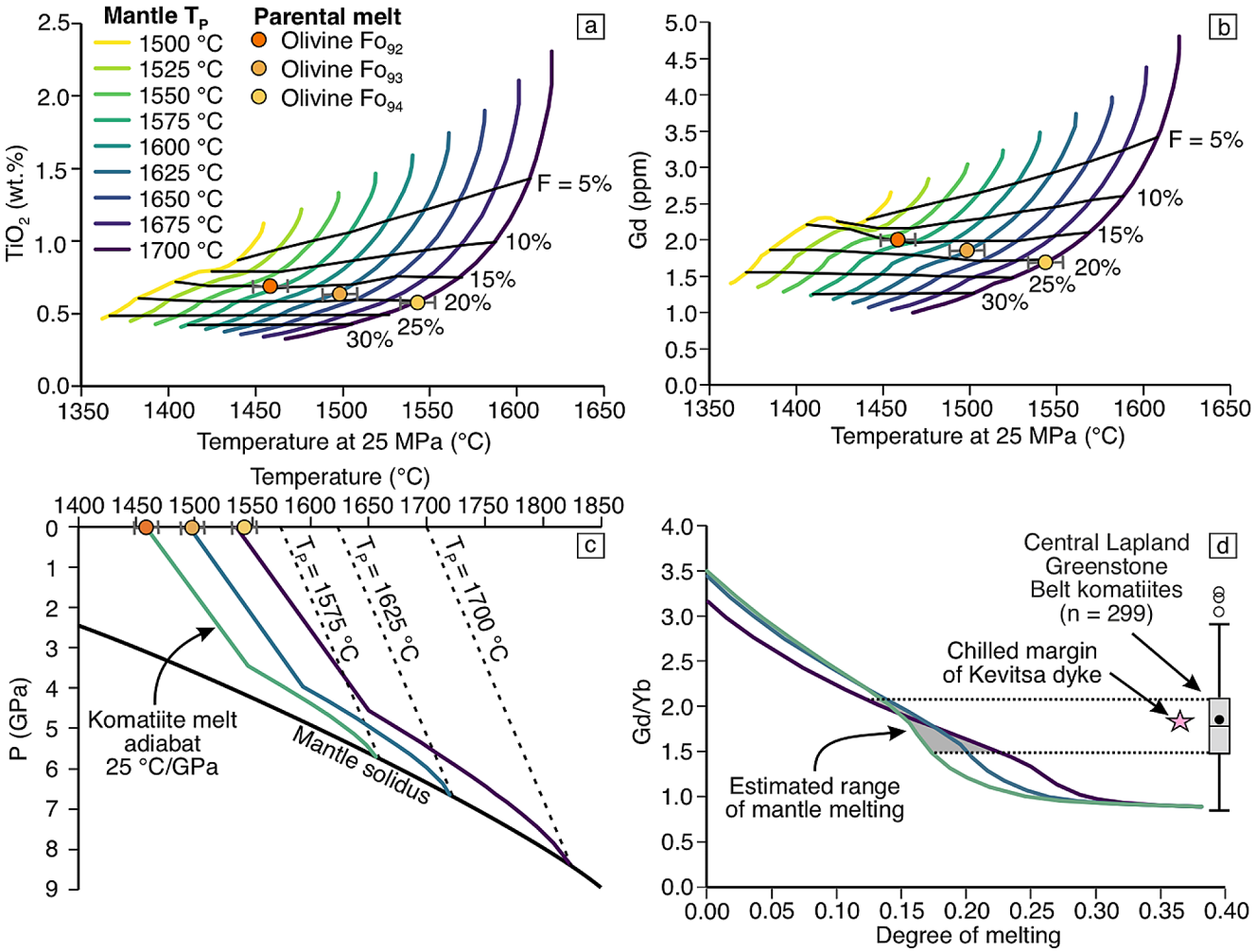

Fig. 3 REEBOX PRO simulation results and parental melts in equilibrium with Fo_{92}, Fo_{93}, and Fo_{94} olivine shown on a temperature vs. TiO_2 (**a**), Gd (**b**), and pressure (**c**) diagrams as well as on a degree of melting vs. Gd/Yb diagram (**d**). The temperatures at 25 MPa on **a** and **b** were calculated for the primary mantle melts formed with different mantle potential temperatures (T_P) by adiabatically decompressing them from their formation depths to 25 MPa using the komatiitic melt adiabat of 0.25 °C/MPa (Miller et al. 1991). The corresponding P-T paths are visible on the diagram **c** for selected simulations. The uncertainties of the parental melt temperatures have been estimated based on the reported analytical uncertainties of olivine measurements used to constrain the parental melt. The analytical uncertainties of TiO_2 and Gd are smaller than the size of the symbols. The natural data on **d** indicates only the Gd/Yb, not the degree of melting, and is from Hanski et a. (2001), Hanski and Kamenetsky (2013), Törmänen et al. (2016), Patten et al. (2023), and this study. For the Central Lapland Greenstone Belt komatiites, the circle represents the average, the line within the box represents the median, the lower and upper bounds of the box represent first and third quartiles, respectively, the T-shaped lines represent the minimum and maximum, and the white circles represent the outliers. Three samples with anomalous high Gd/Yb (4.1, 4.2, and 6.7) were omitted from the natural data to compress the y-axis

komatiites on the regional scale (Fig. 3d). The first and third quartiles of the Gd/Yb of the regional CLGB komatiites are reproduced at similar degrees of melting as the other monitored variables (Fig. 3d).

Using the estimated ranges of mantle melting for the PM^{Fo92}, PM^{Fo93}, and PM^{Fo94} based on the REEBOX PRO results, we compare the parental melt compositions to experimentally determined primary mantle melts from pyrolite source (Walter 1998). For SiO_2, Al_2O_3, and FeO^{tot}, all parental melts are well within the range of primary melt compositions (Fig. 4). The TiO_2 contents of the parental melts are slightly lower compared to the experimental data, especially for the lower estimated degrees of melting (Fig. 4). The PM^{Fo92} and PM^{Fo93} have CaO and MgO

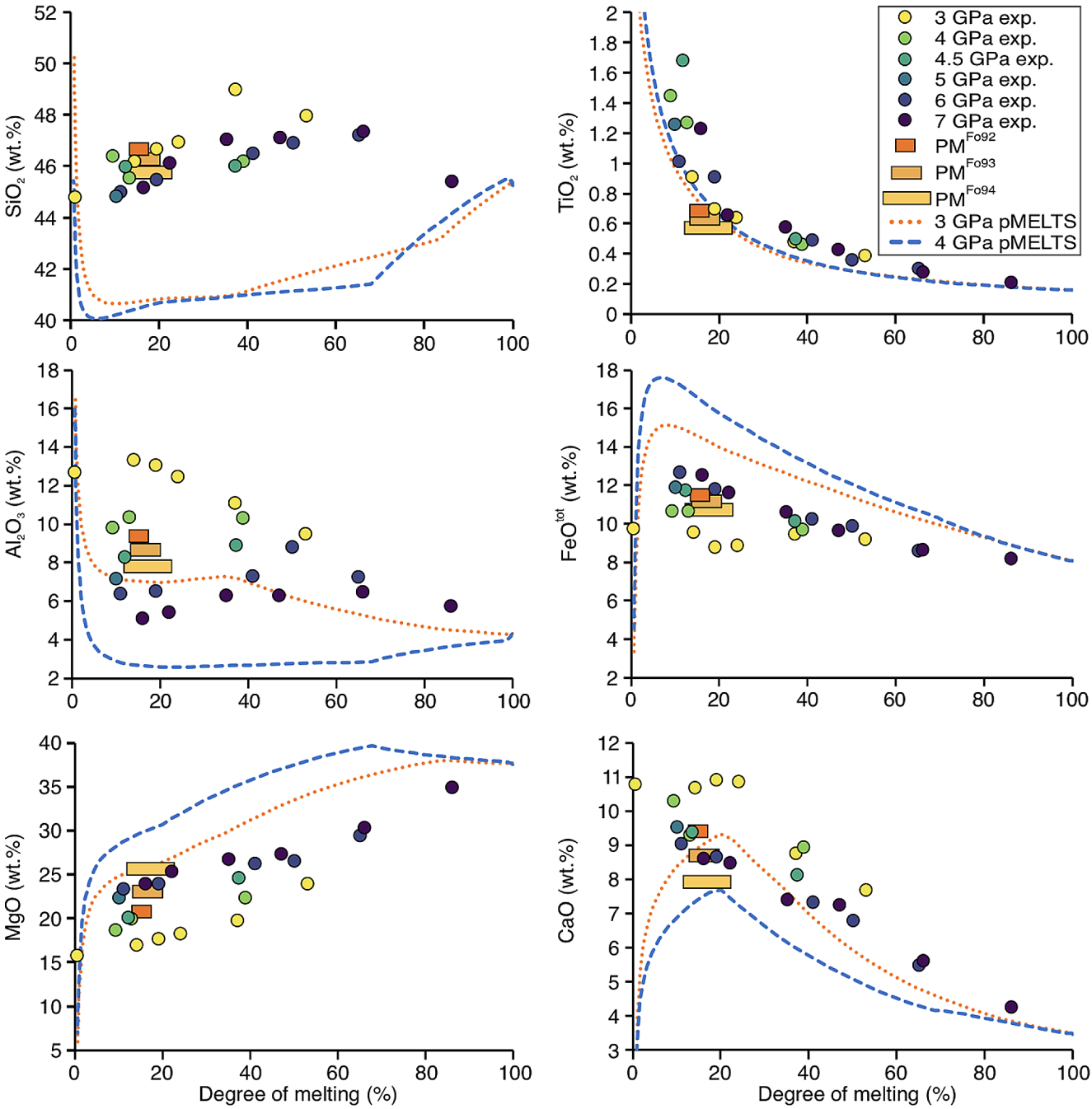

Fig. 4 Degree of melting vs. major element oxide diagrams showing (1) pyrolite mantle melting experiments (exp.) conducted at 3–7 GPa (Walter 1998), (2) parental melt compositions (PM^{Fo92}, PM^{Fo93}, and PM^{Fo94}) of the Central Lapland Greenstone Belt komatiites resulting from the olivine back fractionation calculation, which are coupled with estimated degrees of melting determined based on REEBOX PRO (Brown and Lesher 2016) simulation results (see the text for details), and (3) isobaric CCO-buffered equilibrium crystallization simulations of the same composition as used in mantle melting experiments, using pMELTS (Ghiorso et al. 2002)

contents within the range of experimental data, whereas the PM^{Fo94} has slightly higher MgO content for the lower degrees of melting and lower CaO contents regardless of the degree of melting. Compared to the pMELTS simulations, which were conducted to reproduce the 3 GPa and 4 GPa experiments of Walter (1998), all parental melts produce an overall better fit to the experimental data (Fig. 4).

Under the final P-T conditions of mantle melting, the PM^{Fo92}can dissolve a maximum of 1172 ppm of S (Table 2). With the estimated degree of mantle melting between 15 and 18% and S content of the mantle source in the range of 150–200 ppm, the S content of primary mantle melt can be bracketed in between 856 and 1172 ppm (Table 2). With 150–200 ppm S in the mantle source, sulfide is completely dissolved in the primary melt when the degree of melting reaches 15–17%. In the case of the PM^{Fo93} and PM^{Fo94}, the SCSS depends on the calculated Ni content of the parental melt. The PM^{Fo93} has SCSS of 1174 ppm in the final mantle conditions, when the Ni content of the melt is 882 ppm, whereas with the higher Ni content of 1086 ppm, the SCSS is 974 ppm (Table 2). The lowest initial S content of the PM^{Fo93} is 750 ppm and it is reached when the degree of melting is 20% and S content of the mantle source 150 ppm. With the lower Ni content of 1033 ppm, the PM^{Fo94} can dissolve 1134 ppm S in the final mantle conditions and with the higher Ni content of 1292 ppm, the maximum S content is 912 (Table 2). When the degree of mantle melting is highest and the S content in the mantle lowest, the minimum S content of the PM^{Fo94} is 680 ppm.

Fractional crystallization simulation

The input and output files of the fractional crystallization simulations are included in the Supplementary Materials 3–7. The parental melts PM^{Fo92}, PM^{Fo93}, and PM^{Fo94} produce identical liquid lines of descent for the major element oxides when they reach a common temperature range, hence we describe them collectively here. The liquidus temperatures of the PM^{Fo92}, PM^{Fo93}, and PM^{Fo94} are 1457 °C, 1498 °C, and 1544 °C, respectively. Olivine is the liquidus phase and controls the liquid line of descent between 1544 °C and 1372 °C, which is followed by co-crystallization of olivine and Cr-spinel until 1208 °C. Olivine/Cr-spinel mass ratio remains constant at around 45, meaning that olivine fractionation is the main controlling factor for most of the major element oxides in the residual melt. Clinopyroxene becomes stable at 1203 °C and plagioclase at 1193 °C. Clinopyroxene/plagioclase mass ratio is roughly one, while olivine becomes a minor phase with 5–8 times lower mass compared to the two. Olivine crystallization ceases when temperature reaches 1163 °C leaving the final crystallization assemblage of Cr-spinel, clinopyroxene, and plagioclase before the simulation stops at 1150 °C. In the high-pressure stage (1.2 GPa) of the two-stage simulation conducted only with the PM^{Fo92} composition, Cr-spinel is the liquidus phase at 1565 °C. Orthopyroxene starts to co-crystallize with Cr-spinel from 1560 °C and we terminated the high-pressure stage at 1525 °C when 10 wt% of the system has crystallized. Following the high-pressure stage, the residual melt was depressurized to 25 MPa at which stage olivine becomes the only stable phase as in the one-stage simulations. In the case of major element oxides, the liquid and solid lines of descent are nearly identical (overlapping with the selected symbol size) compared to the one-stage simulations at 25 MPa, hence we only review the results of the one-stage simulations in detail here.

The liquid line of descent is presented on Fenner (MgO vs. major element oxide) diagrams (Fig. 5). The liquid line of descent is monotonously linear for nearly all the major element oxides for the part when olivine ± Cr-spinel are crystallizing (Fig. 5). The exceptions are FeO^{tot} content with slight curvature related to the continuously decreasing MgO/FeO of olivine and Cr_2O_3 content, which starts to decrease when Cr-spinel becomes stable (Fig. 5). The sudden change in the slope of the liquid line of descent at MgO content of 9.3 wt% is related to the stabilization of clinopyroxene and subsequently plagioclase (Fig. 5). The liquid line of descent shows major element oxide contents that are well comparable to those CLGB komatiites that have MgO content in the range of 9.3–25.7 wt% (Fig. 5). The CLGB komatiites with MgO content > 20.6–25.7 wt% have major element oxide

Table 2 Final mantle melting conditions for each parental/primary melt composition and accordingly calculated sulfur content at sulfide saturation (SCSS) and S contents in the melt. Two different ranges for S content has been calculated for PM^{Fo93} and PM^{Fo94} depending on the Ni content of the melt

Simulation	Mantle T_P (°C)	Final pressure of melting (GPa)	Final temperature of melting (°C)	Ni content of melt (ppm)	SCSS (ppm)[2]	S in melt (ppm)
$PM^{Fo92,\ 1}$	1575	3.0	1530	816	1172	857–1172
PM^{Fo93}	1625	4.0	1595	882	1174	750–1174
PM^{Fo93}	1625	4.0	1595	1086	974	750–974
PM^{Fo94}	1700	4.6	1650	1033	1134	680–1134
PM^{Fo94}	1700	4.6	1650	1292	912	680–912

[1]Parental/primary melt in equilibrium with indicated olivine composition

[2]Sulfur content at sulfide saturation. Calculated using the equation of Smythe et al. (2017)

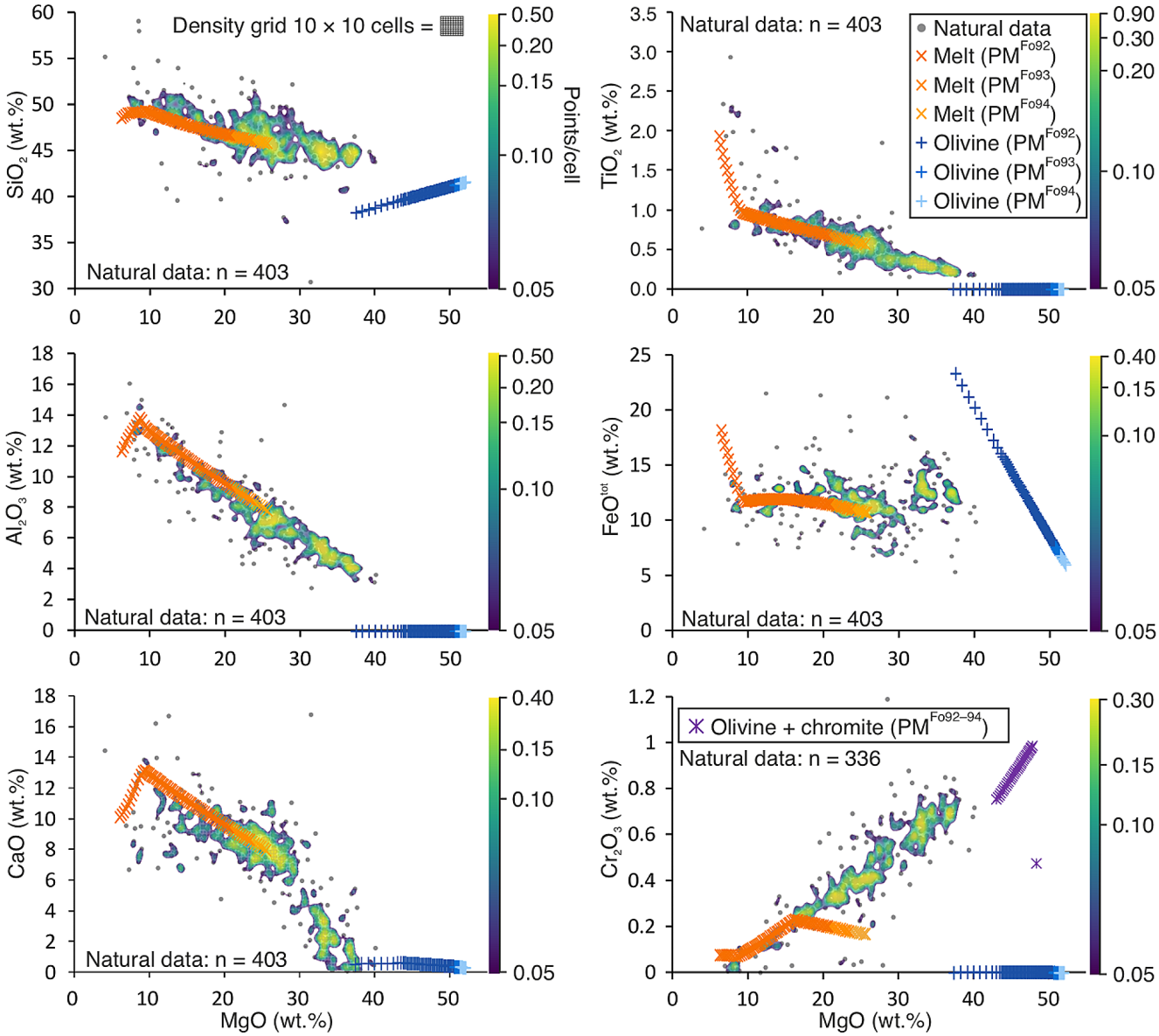

Fig. 5 Fenner diagrams showing selected major element oxide contents for melt and olivine produced in fractional crystallization simulations conducted isobarically at 25 MPa using Magma Chamber Simulator (MCS). The natural data represents komatiitic lavas and associated cumulates from the Central Lapland Greenstone Belt. Bulk compositions of olivine and chromite formed in cotectic proportions are shown on the MgO vs. Cr_2O_3 diagram. The density contours (points/cell) for the natural data were calculated using ioGAS (version 8.0) using the grid density (same for all the diagrams) shown on the MgO vs. SiO_2 diagram

contents that plot mainly between the liquid line of descent and the simulated olivine compositions (Fig. 5).

Within the range of selected initial Ni contents, the one- and two-stage simulations produce liquid lines of descents for Ni, which are well within the range of Ni contents measured from the CLGB komatiites (Fig. 6). In the two-stage simulation olivine has higher Ni-content compared to olivine in the one-stage simulation conducted with the same parental melt PM^{Fo92} (Fig. 6a-b). The reasons for the higher Ni content are the mild incompatibility of Ni to the forming high MgO orthopyroxene ($K^{Ni}_{D_{opx-melt}}$ = 0.62–0.67) and the formation of slightly less forsteritic first olivine ($Fo_{91.4}$) to which Ni is more compatible compared to the more forsteritic olivine ($Fo_{92.1}$) in the one-stage simulation. The majority of the natural komatiite samples have Ni and MgO contents between those of the simulated melt and olivine as expected for olivine-cumulates with variable amounts of interstitial melt (Fig. 6). All simulations produce olivine with composition mostly within the range of natural olivine data from Kevitsa and Sakatti (Fig. 6). Additionally, the natural olivine shows dense populations with clearly lower Ni

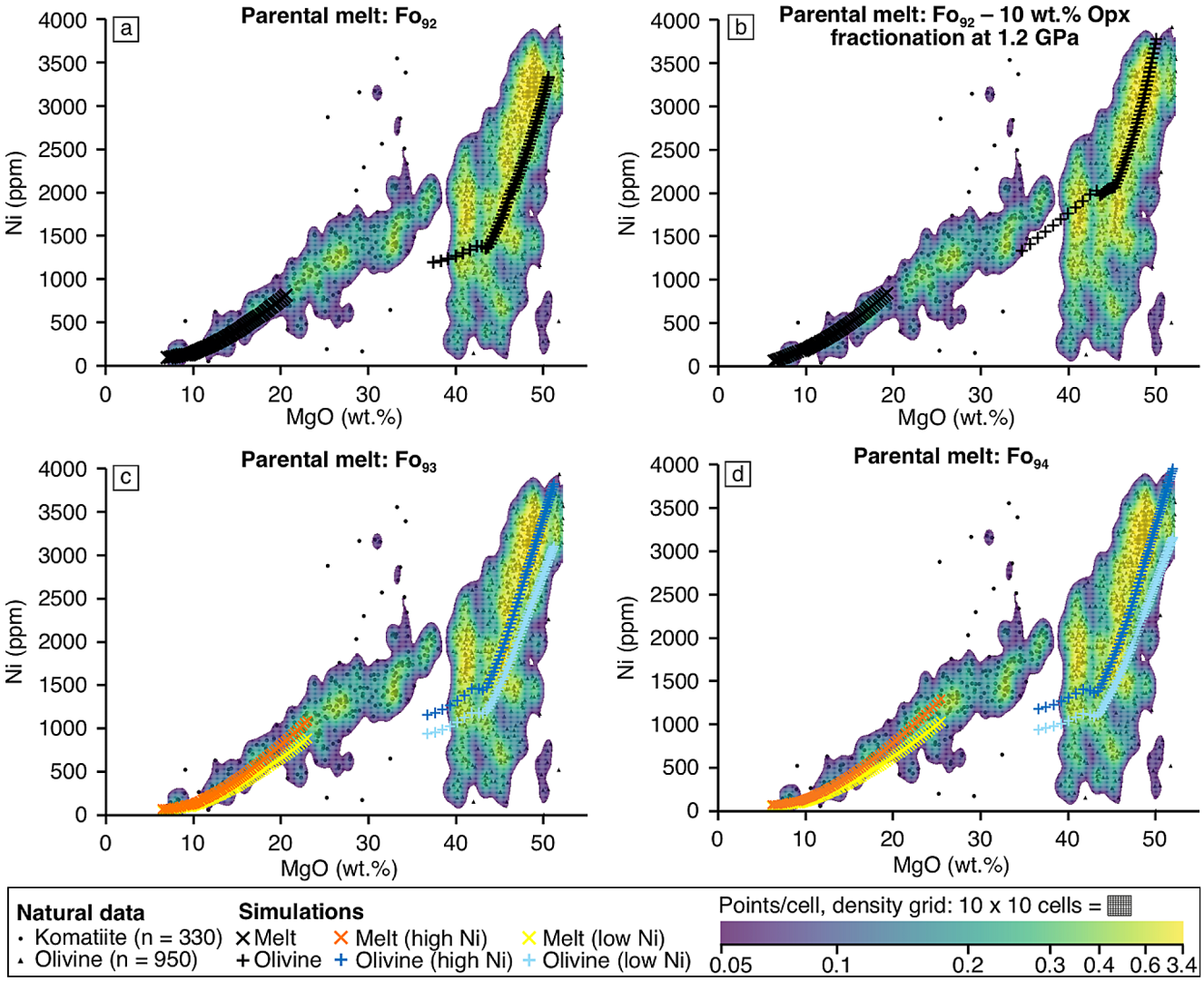

Fig. 6 MgO (wt%) vs. Ni (ppm) diagrams showing the melt and olivine compositions formed in the simulations conducted at 25 MPa with the PM^{Fo92} (**a**-**b**), PM^{Fo93} (**c**), and PM^{Fo94} (**d**) parental melts. In the two-stage simulation shown on **b** the parental melt PM^{Fo92} has fractionally crystallized Cr-spinel and orthopyroxene at 1.2 GPa but only the 25 MPa stage, where olivine is stable, is shown. The simulations were conducted using the Magma Chamber Simulator. The whole-rock composition of komatiites and olivine compositions from the Central Lapland Greenstone Belt are shown on all diagrams. Two outliers from whole-rock dataset were excluded to compress the size of the y-axis: one with 6548 ppm Ni at 25.1 wt% MgO and one with 4943 ppm Ni at 29.5 wt% MgO. Both are peridotite samples with high S content from the Lomalampi area (Törmänen et al. 2016). The density contours (points/cell) for the natural data were calculated using ioGAS (version 8.0)

contents (< 1000 ppm) compared to the simulated olivine compositions at the same MgO content (Fig. 6).

For Cu, natural reference data from whole rock samples are highly scattered (Table S1–2), likely reflecting sulfide removal and accumulation or post-magmatic hydrous alteration (see Le Vaillant et al. 2016), hence these data are omitted from the comparison with the simulation results. The Kevitsa dyke, which was used to calculate the parental melt compositions, has well-preserved magmatic minerals and was demonstrably sulfide-undersaturated during fractionation (see Puchtel et al. 2020) and hence it was included for comparison. In addition, chromite-hosted melt inclusions from the CLGB komatiites (Hanski and Kamenetsky 2013) were included as they are considered less likely to be affected by post-magmatic alteration and sulfide accumulation. The Kevitsa dyke and the melt inclusions contain similar order of magnitude of Cu compared to the fractionally crystallizing melt produced in the one-stage simulations, although clear deviations from the expected fractionation towards higher and lower Cu contents can be observed for some samples (Fig. 7).

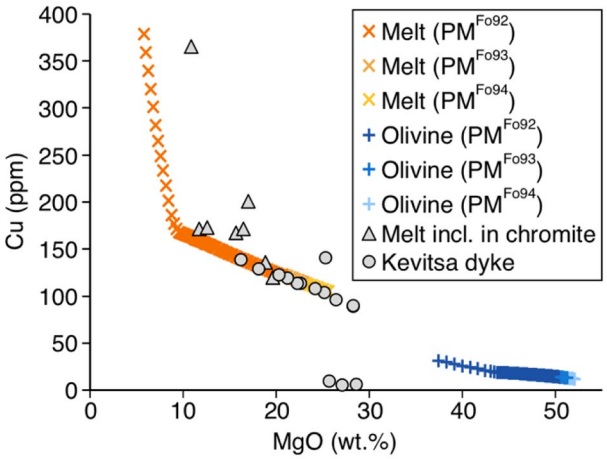

Fig. 7 A diagram showing the Cu content of melt and olivine produced in fractional crystallization simulations conducted with parental melts PM^{Fo92}, PM^{Fo93}, and PM^{Fo94} using Magma Chamber Simulator. Kevitsa dyke data are from Puchtel et al. (2020). Chromite-hosted melt inclusions (incl.) are from komatiitic rocks from the Central Lapland Greenstone Belt (Hanski and Kamenetsky 2013)

Sulfide saturation calculations

The difference in the SCSS between the one- and two-stage fractional crystallization simulations conducted with the PM^{Fo92} is insignificant for our purposes as both lead to saturation of equilibrium sulfide melt with nearly identical Ni/Cu and at similar melt MgO content. Hence only the results of the simpler one-stage simulation are considered in detail here. At 25 MPa, all parental melts have ca. 110–280 ppm higher SCSS at liquidus compared to the final P-T conditions in the mantle. The differences between the SCSS in the mantle and crustal conditions are due to decrease of pressure and temperature (adiabatic cooling) as well as consequent change in equilibrium sulfide composition (especially temperature affects Ni and Cu partitioning to sulfide). The S contents of the simulated fractionally crystallizing melts are similar to the S contents measured from chromite-hosted melt inclusions from the CLGB komatiites ($n = 20$) with the exception of four data points with clearly higher or lower S contents (Fig. 8a-c). Whole-rock S contents measured from the CLGB komatiites were omitted from the comparison because these are more likely to be affected by metamorphic remobilization, sulfide removal or accumulation, and degassing than the melt inclusions. With the higher initial S content of 1172 ppm, the PM^{Fo92} reaches sulfide saturation when MgO content is 11.9 wt%, whereas with the lower initial S content of 857 ppm the melt has 8.7 wt% MgO at sulfide saturation (Fig. 8a). With the lower initial Ni content, the PM^{Fo93} has initial S content between 750 ppm and 1174 ppm (Table 2) and it reaches sulfide saturation at 7.9 wt% and 12.0 wt% MgO, respectively (Fig. 8b). When the PM^{Fo93} has the higher initial Ni content, the initial S content is 750–974 ppm (Table 2) and sulfide saturation occurs when MgO is between 8.2 and 10.1 wt% (Fig. 8b). The PM^{Fo94} with lower initial Ni content has initial S content of 680–1134 ppm (Table 2) and the residual melt reaches sulfide saturation at MgO content of 7.9–12.8 wt% (Fig. 8c). With the higher initial Ni content, the PM^{Fo94} has initial S content of 680–912 ppm (Table 2) and sulfide saturation is reached when the melt has MgO content of 8.2–10.3 wt% (Fig. 8c). Between the earliest and latest sulfide saturation, the residual melt of the PM^{Fo92} is in equilibrium with sulfide having Ni/Cu ratio of 1.8 and 0.6, respectively (Fig. 8d). For the PM^{Fo93}, the equilibrium sulfide has Ni/Cu of 0.2–1.5 when the initial Ni content of the parental melt is low, whereas with the high initial Ni content, the Ni/Cu of the equilibrium sulfide is 0.4–1.0 (Fig. 8d). The Ni/Cu of the equilibrium sulfide for the PM^{Fo94} is 0.3–1.8 with lower initial Ni content and 0.4–1.0 with the higher initial Ni content (Fig. 8d). The final sulfide assemblage for each parental melt is expected to be dominated either by pentlandite (Ni/Cu > 1) or chalcopyrite (Ni/Cu < 1) with pyrrhotite as an additional main sulfide phase (Fig. 8d).

Discussion

Estimating the uncertainties of the simulations

As any simulations, ours are subject to several uncertainties related to the selection of starting parameters, to the choices of simulated processes (e.g., closed vs. open system, fractional vs. equilibrium melting/crystallization), to the capabilities of the chosen software to reproduce experimental data, and to the uncertainties of the experimental data used to calibrate the software. After all, simulations can never be more than simplified approximations of complex natural systems but their utility for petrological research is in making internally consistent quantitative estimations of heat and mass transfer as well as phase equilibria. Making a full analysis of all uncertainties related to the software and their experimental input data is out of the scope of this study. Previous benchmarking of REEBOX PRO (Brown and Lesher 2016) as well as MELTS and MCS (e.g., Ghiorso and Sack 1995; Bohrson et al. 2014; Ghiorso and Gualda 2015) suggests that these software reproduce experimental and natural data reasonably well and can provide meaningful approximation of the behavior of natural systems. Here we evaluate our choice of starting parameters and the ability of MELTS to produce a reasonable liquid line of descent for our komatiite, which depends on the capability of MELTS to reproduce the olivine and Cr-spinel compositions and their relative stabilities. In our simulations, this capability

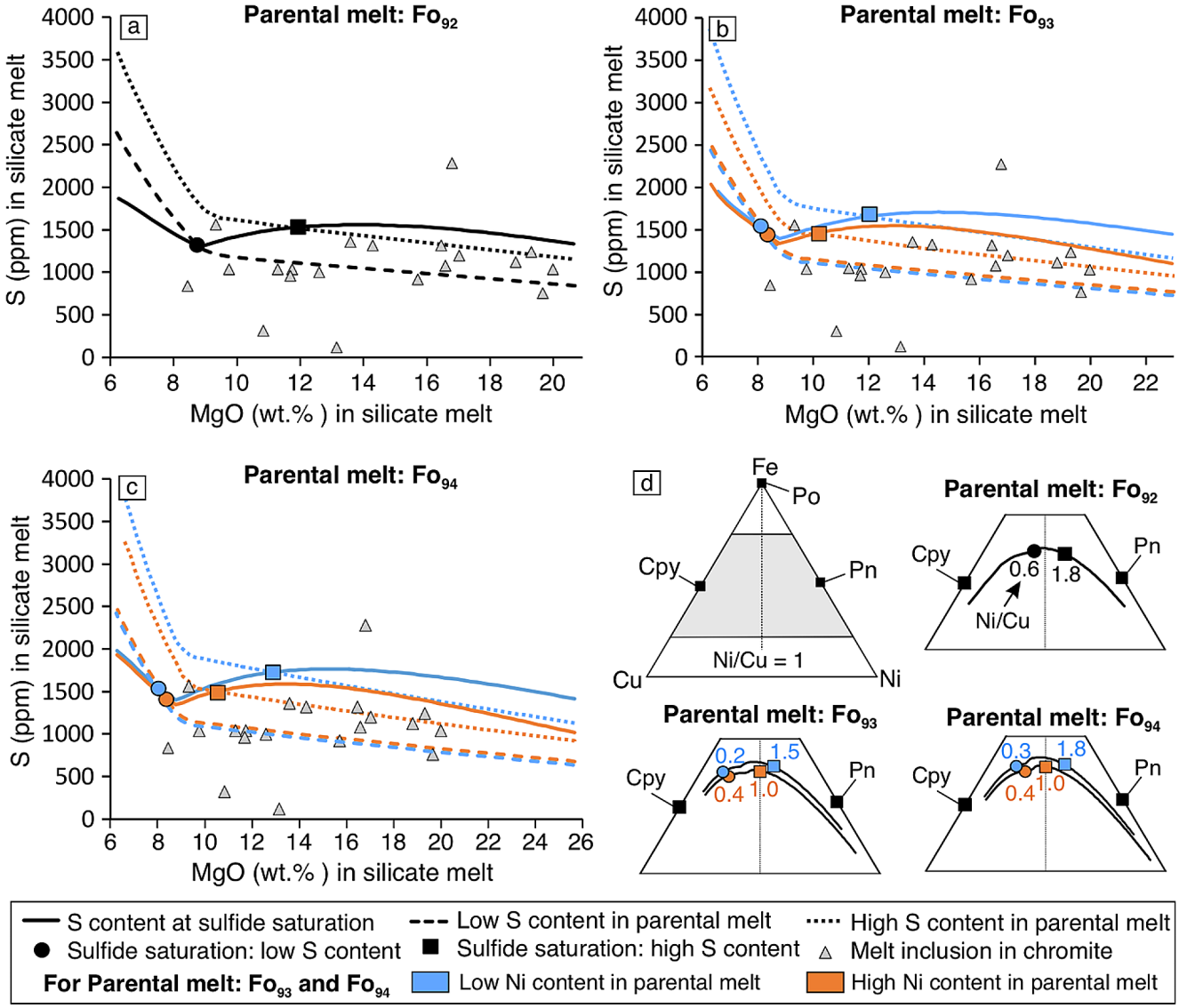

Fig. 8 **a-c** MgO content in silicate melt vs. S content in silicate melt diagram showing data from the simulations and natural melt inclusions measured from chromite grains that originate from Central Lapland Greenstone Belt komatiites (Hanski and Kamenetsky 2013). Sulfur content at sulfide saturation has been calculated using the equation of Smythe et al. (2017). **d** Equilibrium sulfide compositions shown on Fe-Cu-Ni ternary diagrams for each parental melt. The numbers next to the symbols indicate Ni/Cu of sulfide in equilibrium with the silicate melt based on the parameterization of Kiseeva and Woods (2015). Compositions of chalcopyrite (Cpy), pyrrhotite (Po), and pentlandite (Pn) are shown on the ternary diagrams

affects the composition of the back-calculated parental melt and the compositions produced in the fractional crystallization simulations and their derivative calculations related to S content and sulfide saturation. The stabilities of clinopyroxene and plagioclase are less important as they are stable only in the very late stage of the simulation.

We compare our simulation results to the experiments of Matzen et al. (2011), which were conducted with a synthetic "Hawaiian" picrite in a temperature range of 1300–1600 °C, at 1 atmosphere pressure, and with fO_2 constrained to the FMQ buffer (their experiments with other fO_2 buffers are not considered here). The starting material of the experiments produces closely similar liquid line of descent compared to our simulated parental melt (Fig. 9) apart from TiO_2, which has higher concentration (by ca. 1 wt%), and CaO, which has lower concentration (by ca. 1 wt%), in the synthetic picrite. Because TiO_2 and CaO are not main structural components in olivine or Cr-spinel, we suggest that their effects on the relevant phase compositions can be neglected. We tested the effects of the 25 MPa difference in pressure and the one log unit difference in fO_2 between FMQ and ΔFMQ -1 on the olivine composition for the synthetic picrite of Matzen et al. (2011) in MELTS. The test suggests that there is no difference on olivine composition with the relevant pressure

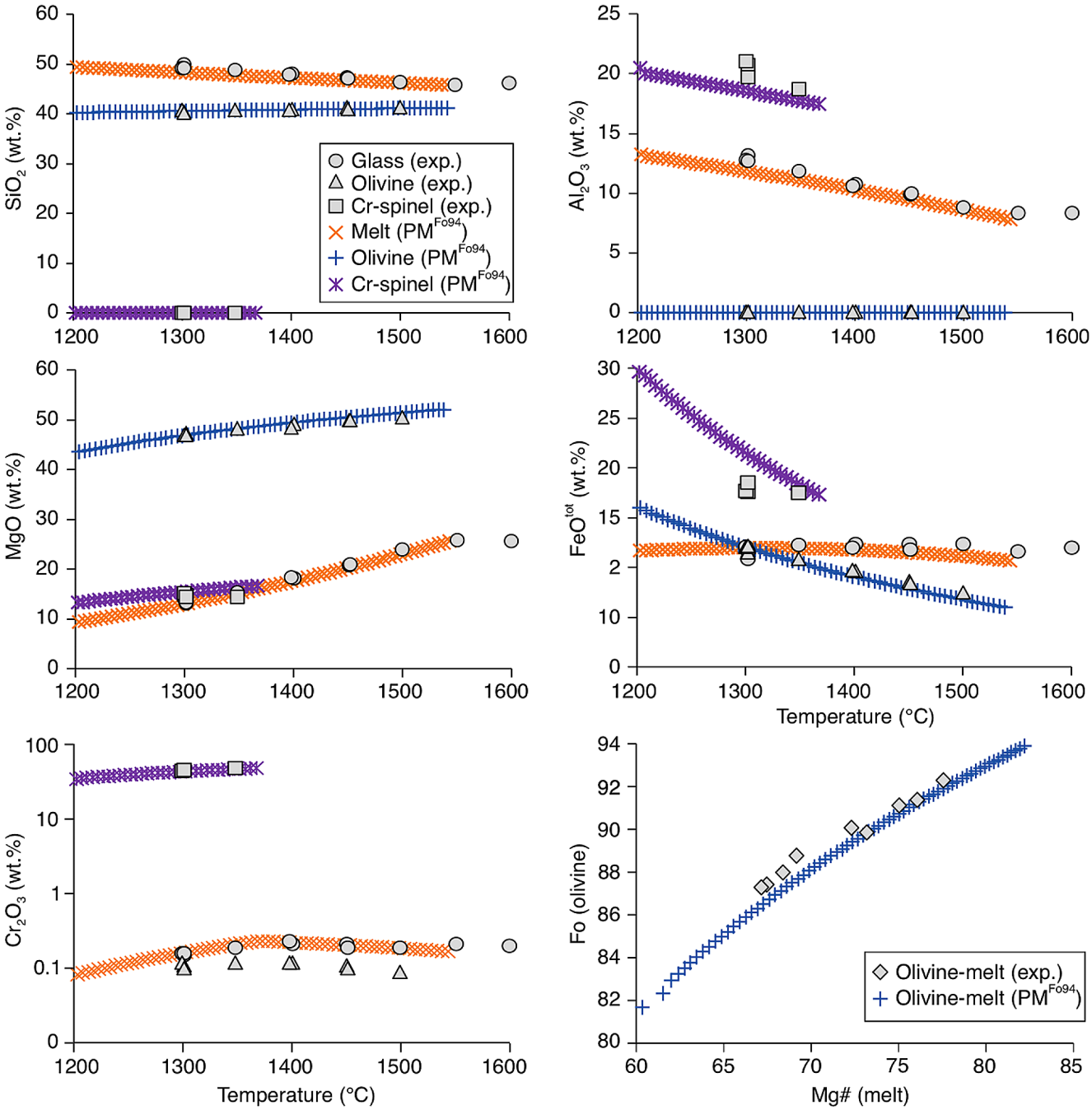

Fig. 9 Experimental data (Matzen et al. 2011) and fractional crystallization simulation results shown on temperature vs. major element oxide and Mg# vs. forsterite (Fo) number of olivine diagrams. The experiments (exp.) have been conducted with a synthetic "Hawaiian" picrite under atmospheric pressure and fO_2 buffered to FMQ. The simulations were conducted with Magma Chamber Simulator using the Central Lapland Greenstone Belt komatiite parental melt in equilibrium with olivine Fo_{94} (PM^{Fo94}) as the starting composition. Pressure in the simulations was 25 MPa and the original fO_2 of the parental melt is -1.3 log units below the FMQ buffer. In the simulation, fO_2 is not buffered

range and that the difference in fO_2 causes Fo to change by 0.5 units, which is close to the analytical uncertainty of EMPA and hence considered negligible.

The relative stabilities and compositions of olivine and Cr-spinel are similar between the experiments and simulations (Fig. 9). The capability of MELTS to predict the relative stabilities of olivine and Cr-spinel is important as it validates that olivine is the liquidus phase of the Kevitsa dyke parental melt. This is also compatible with the observation that the largest olivine crystals with highest Fo are

free of Cr-spinel inclusions in the Kevitsa dyke (Puchtel et al. 2020). Considering that the experiments were more oxidized compared to the simulations, it can be concluded that MELTS overpredicts Cr-spinel stability in our simulations (Fig. 9) as already shown in several other studies (e.g., Hirschmann et al. 1998; Waterton et al. 2020). However, with the olivine/Cr-spinel mass ratio in the simulations being ca. 45, the Cr-spinel stability has significant effect only for Cr_2O_3 content of the residual melt. Because Cr_2O_3 content is not considered in the SCSS parameterization of Smythe et al. (2017) and because the effect of Cr-spinel on Ni content is less than the analytical uncertainty related to Ni measurements, Cr-spinel stability is not considered to significantly affect the simulation results. As the experimental and simulated olivine and melt compositions are closely similar (Fig. 9), we suggest that MELTS is capable of producing reasonably accurate compositions for the CLGB komatiites.

The most important factors controlling the Ni content of the simulated melt and olivine are the chosen partition coefficient and the representativeness of the Ni content of the most primitive olivine. Several studies have shown that Ni partitioning to olivine changes as a function of composition or temperature (e.g., Arndt 1977; Li et al. 2001; Matzen et al. 2013, 2017). The reliability of these $K^{Ni}_{D_{ol-melt}}$ formulations depends on the experimental or natural datasets as well as the precision and accuracy of measurements used in the calibration. With the high-Ni olivine in the CLGB komatiites, even a seemingly small difference of 0.5 in the initial $K^{Ni}_{D_{ol-melt}}$ changes the Ni content in the melt by hundreds of ppm, which is much larger than the analytical uncertainty of the whole-rock Ni measurements. Producing a meaningful simulation for Ni is highly dependent on the choice of the $K^{Ni}_{D_{ol-melt}}$ parameterization. Matzen et al. (2013) provide a comparison between 16 different $K^{Ni}_{D_{ol-melt}}$ parameterizations and experiments showing that few are in good agreement in the temperature range of 1400–1550 °C. Hence, testing the several parameterizations is not necessary for our simulations. We argue that the most appropriate $K^{Ni}_{D_{ol-melt}}$ formulation for our simulations is the one of Matzen et al. (2017), which has been constrained in a similar manner with the one of Matzen et al. (2013) but with more data. As the chosen parameterization shows good fit to the natural whole-rock and olivine data used to validate our simulation results (Fig. 6), we suggest the chosen $K^{Ni}_{D_{ol-melt}}$ formulation is appropriate. Because Cu and REE are incompatible elements and remain in low concentrations throughout our simulation, changing their partition coefficients would not affect the simulation results beyond the analytical uncertainty of these elements. For example, using a bulk partition coefficient of zero for Cu, would change Cu concentration in the residual melt only a few ppm. Hence, we do not provide a detailed analysis of the effect of these partition coefficients.

Considering the arguments above, we suggest that the use of MELTS compiled with the chosen partition coefficients produces a reasonable parental melt and its fractional derivatives in our simulations. The adopted starting parameters also affect the simulation results. We chose to test only a single composition, the Kevitsa dyke chilled margin (Puchtel et al. 2020), in equilibrium with the three olivine compositions (Fo_{92}, Fo_{93}, and Fo_{94}) to calculate the most primitive melt compositions, which we assumed to be suitable for all CLGB komatiites on the regional scale. We rationalize our choice of the Kevitsa chilled margin as the common parental melt for all CLGB komatiites by referring to the philosophical argument known as the Occam's razor, which in our context, means that for any simulation, the number of variables should be kept to minimum whenever possible. Because the simulations show a reasonably good fit to the full reference dataset using the parental melts defined based on the one selected natural composition, there is no necessity to constrain and test other parental melts. We do not claim that our parental melt composition is strictly valid for all CLGB komatiites but that it is good enough approximation to make a meaningful petrogenetic model.

The correctness of the choice related to the most primitive olivine depends on the identification of the truly most primitive olivine of the CLGB komatiites as well as to the analytical uncertainty of the olivine measurements in our reference dataset. Identifying the most primitive olivine that originally crystallized from the parental melt can be impossible from the natural rock record. This is because the most primitive olivine population might not reach the final level of emplacement or might be so scarce that it evades sampling. Olivine also equilibrates, to some degree, with the residual melt after its formation, which erases the original composition. Moreover, olivine can become inherited from the mantle source (e.g., Herzberg et al. 2007) or its composition can become "too primitive" by assimilation of dolomite (e.g. Holness 2000). To account for the uncertainty in the representativeness of the most primitive olivine and for the possible regional scale heterogeneity, we tested the three different liquidus olivine compositions (Fo_{92}, Fo_{93}, and Fo_{94}) for our parental melts. As all the parental melts have identical liquid and solid lines of descent for the major element oxides on within the common temperature range, the most important differences with the chosen olivine are related to the Ni contents and the estimated mantle melting conditions.

For a reason not discussed in the original data sources, the scatter of Ni content for Fo_{93} and Fo_{94} olivine in the Kevitsa dyke greatly surpasses the analytical uncertainty with the difference in Ni content with constant Fo being

nearly 1000 ppm (Nicklas et al. 2019; Puchtel et al. 2020). Based on the available data, we cannot deduce if the heterogenous Ni contents result from more efficient equilibration of Ni in smaller grains, poor efficiency of Ni equilibration throughout the size of the dyke, or some other unknown process. This uncertainty in the Ni content leads to the largest uncertainty for the simulated Ni content in olivine and melt (Fig. 6), and consequently on the S content, SCSS, and saturation of the equilibrium sulfide (Fig. 8). Hence, we have taken this uncertainty into account in all relevant simulations. Further studies could help to narrow down this uncertainty if the reason for the heterogeneous Ni contents in the reference olivine grains could be unraveled. We conclude that our simulation are expected to provide a reasonably good approximation of the chemical fractionation for the CLGB komatiites to make tentative quantitative estimations of the thermodynamic variables (importantly P, T, and composition) related to the mantle melting and crustal fractionation processes.

Mantle melting conditions

The results of the parental melt calculations by olivine addition as well as the subsequent estimation of the mantle melting conditions are highly dependent on the choice of the most primitive olivine composition. Reference data from the melt-dominated CLGB komatiites is lacking for the most parts of the CLGB. Most primitive olivine populations from the Kevitsa dyke have $Fo_{93–94}$ (Nicklas et al. 2019; Puchtel et al. 2020) and the most primitive Ni-undepleted olivine in Sakatti has Fo_{92} (Brownscombe et al. 2015; Höytiä unpublished).Simulations conducted with REEBOX PRO show that the parental melts PM^{Fo92}, PM^{Fo93}, and PM^{Fo94} could have derived from a single mantle source, which had variable mantle T_P in the range of 1575–1700 °C (Fig. 3). Only in the case of PM^{Fo94}, the mantle melting simulation fails to produce are a concurrent solution for TiO_2, Gd, and Gd/Yb within the range of analytical uncertainty of these elements in the measurements of the Kevitsa dyke chilled margin (Puchtel et al. 2020). However, the difference between the solutions produced with TiO_2, Gd, and Gd/Yb is < 2% for the degree of mantle melting, which corresponds to P and T differences of 0.2 GPa and 10 °C, respectively, in the mantle melting column. Given the uncertainties related to the true composition of the mantle source, we consider these differences acceptable. The major element contents of the PM^{Fo92}, PM^{Fo93}, and PM^{Fo94} are mostly within the range of the experimental results of pyrolite mantle melting experiments (Walter 1998; Fig. 4), which strengthens the view that these compositions could be representative for both the parental and primary melts. Only the CaO content of PM^{Fo94} is considerably lower compared to the mantle melting experiments and would require degree of melting to reach roughly 40 ± 10% (Fig. 4). This higher degree of melting is compatible with the other experimental major element contents (Fig. 4) and with the previous estimation of the mantle melting reaching 49% with T_P of 1763 °C (Puchtel et al. 2020). However, with such high degree of melting, the partial melt would have lower Gd and Yb contents compared to the parental melt and the REE pattern should become similar with the mantle source (e.g., Gd/Yb < 1 for depleted mantle sources, see Fig. 3d). In addition, the S content of the primary melt was constrained to 420 ppm (Puchtel et al. 2020), which in comparison to most of the chromite-hosted melt inclusions from the Jeesiörova komatiites (Hanski and Kamenetsky 2013; Fig. 8), would lead to 300–700 ppm lower S content in the fractionally crystallizing melt. We consider it possible that the parental melt of Kevitsa dyke formed by much higher degree of melting compared to the komatiites in Jeesiörova, which could explain the differences in the S contents. However, the abovementioned discrepancies in the REE contents cannot be explained by the higher degree of melting. This could possibly be explained by the suggested earlier melt extraction event (Puchtel et al. 2020) combined with the complex re-fertilizing and re-melting processes of a possibly pyroxenite-mixed depleted mantle source as suggested to be required for the characteristic MREE-enriched pattern of the CLGB komatiites (Hanski and Kamenetsky 2013). Alternatively, the discrepancy in the CaO content of our PM^{Fo94} composition and the experiments, which were conducted with an undepleted pyrolite composition (Fig. 4), could be explained by an earlier melt extraction event as the low degree mantle partial melts are more than three times enriched in CaO relative to the source composition (Walter 1998). For now, we consider that the parental melt in equilibrium with Fo_{94} olivine could have formed either if the mantle T_P was 1763 °C and the degree of melting 49% or if the mantle T_P was 1700 °C and the degree of mantle melting 14–22%. We only consider the latter estimation for the following parts of the discussion.

Based on the available data, there is a difference in the most primitive olivine in the Kevitsa dyke (Nicklas et al. 2019; Puchtel et al. 2020) and in Sakatti (Brownscombe et al. 2015; Höytiä unpublished). We suggest that this is a result of thermal differences (1575–1700 °C) in the otherwise compositionally uniform upwelling mantle source. The hottest part of the upwelling mantle, which forms the PM^{Fo94}, would start melting at 8.5 GPa pressure, corresponding roughly to the depth of 260 km, and the column-accumulated partial melt would get extracted from the source at 4.6 GPa, which corresponds to the depth of 200 km. The PM^{Fo93} forms from the part of the mantle that has T_P of 1625 °C. This portion of the mantle melts from 6.6 GPa (depth of 245 km) to 4.0 GPa (depth of 190 km) before the detachment of the partial

melt. Finally, the portion of the mantle with T_p of 1575 °C, starts to melt at 5.0 GPa (depth of 210 km) and produces a column-accumulated melt composition of the PM^{Fo92} at 3.0 GPa (depth of 165 km). These differences in the mantle melting conditions and degrees of melting are compatible with the variable Gd/Yb in the CLGB komatiites (Fig. 3d), which likely reflect the mantle composition because crustal fractionation should not significantly affect Gd/Yb due to their similar partition coefficients to olivine (Bédard 2005). The suggested thermal heterogeneity could be distributed horizontally and/or vertically within the upwelling mantle column and could cause the spatiotemporal differences in the komatiitic parental melt compositions within the CLGB. In the context of our study, the importance of this heterogeneity is related to constraining reasonable ranges for Ni content in olivine, for Ni and S content of the melt, and for equilibrium sulfide compositions on the regional scale.

Sulfur content of the primary mantle melt

Due to the uncertainties related to S content of the mantle source (Lorand and Luquet 2016) and the degree of mantle melting for each primary mantle melt, we are not able to pinpoint S contents for the corresponding parental melts. Instead, we have bracketed ranges of S contents for the parental melts (Table 2), which show good agreement with the data from the chromite-hosted komatiite melt inclusions (Fig. 8a-c). We suggest that the bracketed ranges are likely more realistic than fixed S contents for the CLGB komatiites on the regional scale and that the differences can be attributed either to slightly heterogeneous S content in the mantle source or to small changes in the degree of mantle melting. If S content of the depleted mantle source varies in between 150 and 200 ppm (Lorand and Luquet 2016), the variability of the initial S content of a sulfide-undersaturated primary melt is 230–360 ppm for the relevant range of melting (14–22%). The effect of 1% difference in the degree of mantle melting on the S content of a sulfide-undersaturated primary melt is 30–100 ppm. Hence, these minor differences lead to variable S contents. Variability in the degree of mantle melting is also compatible with some of the local and regional variations in REE patterns (see Fig. 3d for Gd/Yb) of the CLGB komatiites (Hanski and Kamenetsky 2013). Due to the uncertainties related to degree of mantle melting, and S content of the mantle source, the simulations alone cannot reliably determine if mantle sulfide was fully dissolved during mantle melting on the scale of the whole CLGB. The PGE contents in Kevitsa (Le Vaillant et al. 2016; Puchtel et al. 2020), Lomalampi (Törmänen et al. 2016), and Sakatti (Brownscombe et al. 2015) indicate that total dissolution of mantle sulfide was clearly reached, which means that lowest estimations for the degree of mantle melting based on the simulations are likely underestimations. This interpretation is also compatible with the major element contents of the parental melts, which show better agreement with the mantle melting experiments with higher degrees of melting (Fig. 4). The theoretical maximum contents for S, Cu, and PPGE in mantle-derived melts are reached at the exact stage when all sulfide becomes dissolved as further melting would cause dilution of these elements (e.g., Yao et al. 2018). Based on our simulations, the degree of mantle melting related to the formation of the CLGB komatiites is close to the threshold of total sulfide dissolution. This means that, in comparison with many Archean komatiites that formed by generally larger degrees of mantle melting (25–50%, see e.g., Sossi et al. 2016), the CLGB komatiites required likely less S assimilation to reach early sulfide saturation and were more prone to produce relatively Cu- and PPGE-rich sulfides.

Fractional crystallization of the parental melt

Pressure, temperature, and liquid line of descent control sulfide saturation of a magma experiencing closed-system fractional crystallization. Komatiitic liquid lines of descent are relatively simple compared to more evolved magmatic systems as they are controlled by olivine ± Cr-spinel crystallization for the most part. Overall, the major element data from the CLGB komatiites is chemically clearly more variable, (especially in terms of SiO_2, FeO^{tot}, and CaO) than the simulated liquid line of descents (Fig. 7), which cannot be explained by simple olivine ± Cr-spinel fractionation. Processes that can cause the observed scatter in the reference data include alteration, mineral accumulation, and assimilation. The CLGB komatiites have been variably metamorphosed to serpentinite, and locally to amphibole, and chlorite-bearing rocks on regional and sample scale (e.g., Saverikko 1985; Hanski et al. 2001; Le Vaillant et al. 2016; Törmänen et al. 2016). Serpentinization is generally thought to be isochemical on whole-rock sample scale for most major element oxides but enrichment of SiO_2 and depletion of CaO is sometimes observed in serpentinized rocks (e.g., Deschamps et al. 2013; Malvoisin 2015). The CLGB komatiites show high variability for SiO_2 and CaO at constant MgO content, which cannot be explained by olivine fractionation or accumulation (Fig. 7). We suggest that the observed high SiO_2 and low CaO contents (Fig. 7) are related to serpentinization instead of magmatic processes. Serpentinization and later higher degree metamorphism has likely also affected the highly variable S contents of many of the CLGB komatiites (Table S1–2).

Differentiated komatiitic lava flows and sills with cumulus olivine have been described from the CLGB (e.g., Hanski et al. 2001; Törmänen et al. 2016), which is clearly observable

on the whole-rock composition diagrams. We consider it highly likely that the natural komatiites with higher MgO content than that of the inferred parental melts (20.6–25.7 wt%) contain variable amounts of cumulus grains as these samples are chemically readily explained as mixtures of olivine ± Cr-spinel and melt (Fig. 7). In addition, some of the samples with lower MgO content are likely mixtures of more evolved melt and cumulus olivine ± Cr-spinel, especially the samples with high FeO^{tot}/MgO compared to the simulated liquid line of descent (Fig. 7). The few outliers with too high FeO^{tot} content to be explained by olivine ± Cr-spinel accumulation (Fig. 7) might contain accumulated sulfides. However, without petrographic descriptions and S content data from all these samples we cannot evaluate this in detail. Regardless of the uncertainties, most of the deviations from the liquid line of descent can be readily explained by serpentinization and olivine ± Cr-spinel accumulation. Based on high variability of LREE contents in the CLGB komatiites (La/Sm = 0.1–4.0, Table S1–2), we consider it likely that at least some of the komatiites assimilated crustal rocks but the effects of assimilation on the liquid line of descent of the major element oxides seem to be of secondary importance compared to closed-system crystallization.

We conclude that differentiation of the CLGB komatiites is largely controlled by olivine ± Cr-spinel crystallization as expected for komatiites in general. The simulated quantities of the major element oxides (Fig. 5), Ni (Fig. 6), and Cu (Fig. 7) on the liquid line of descent are well comparable with the natural reference data from the CLGB komatiites. This suggest that our parental melt compositions can be used to calculate a meaningful SCSS and Ni content in olivine for the CLGB komatiites.

Sulfide saturation via fractional crystallization

Here we discuss the timing of sulfide saturation and compositional range of sulfides that are expected to form from CLGB komatiites experiencing strictly closed-system fractional crystallization without the effects of S assimilation from the country rocks. The largest known sulfide ore deposits in CLGB, such as in Kevitsa and Sakatti as well as the smaller Lomalampi sulfide deposit, contain assimilated S (Yang et al. 2013; Törmänen et al. 2016; Luolavirta et al. 2018b; cf., Brownscombe et al. 2015), hence our purpose here is not to explain the compositional variability of the sulfide ore types in detail. Nevertheless, the variation of equilibrium sulfide composition as a function of the timing of sulfide saturation, as discussed below, is a relevant underlying process also for the assimilation-induced sulfide saturation. This is because the degree of fractional crystallization preceding assimilation controls the metal contents of the residual melt and consequently the composition of the precipitating sulfide phase.

In general, sulfide deposits associated with komatiites are Ni-rich and relatively Cu-poor (e.g., Naldrett 2004; Barnes and Lightfoot 2005). In the case of Sakatti and Kevitsa, both Ni-rich and Cu-rich sulfide occurrences have been found, the latter being the dominant type (Yang et al. 2013; Brownscombe 2015, Luolavirta et al. 2018a). In Sakatti, the Cu-rich sulfides have systematically lower IPGE and higher PPGE compared to the Ni-rich sulfides (Brownscombe et al. 2015). The systematic relationship between Ni/Cu and IPGE/PPGE in Sakatti sulfides has been interpreted to result from sulfide melt fractionation (Brownscombe et al. 2015; Fröhlich et al. 2021). In this process, homogeneous sulfide melt first crystallizes to Ni- and Cu-poor monosulfide solid solution (MSS) to which IPGEs are compatible and PPGEs incompatible compared to the residual sulfide melt (e.g., Barnes and Lightfoot 2005; Mungall 2014). Crystallization of the fractionated sulfide melt, now enriched in Ni, Cu, and PPGEs, forms increasingly Ni-rich MSS as temperature decreases, while the residual melt becomes correspondingly Cu and PPGE-rich (e.g., Barnes and Lightfoot 2005; Mungall 2014). Subsequent physical separation of the residual sulfide melt from the MSS, for example by downward percolation to the less dense silicate cumulates, can lead the observed Ni/Cu and IPGE/PPGE systematics.

In our simulations, the onset of sulfide saturation and the Ni/Cu of the forming sulfide depends on the Ni and S contents of the parental melts (Fig. 8). With the bracketed range of initial S contents, both Ni- and Cu-dominant sulfides can precipitate from the PM^{Fo92} (Ni/Cu = 0.6–1.8) as well as from the PM^{Fo93} (Ni/Cu = 0.2–1.5) and PM^{Fo94} (Ni/Cu = 0.3–1.8) when they have low initial Ni contents (Fig. 8d). Paradoxically, the PM^{Fo93} and PM^{Fo94} with higher initial Ni contents, are expected to saturate sulfides with Ni/Cu of 0.4–1.0, meaning that Cu-rich sulfides are more likely to form via closed-system fractional crystallization of these parental melts regardless of their initial S content (Fig. 8d). These results indicate that Ni- and Cu-dominant sulfides are expected to form by fractional crystallization of parental melts with variable initial Ni and S contents, which could be related to a few percent difference in the degree of melting or a few tens of ppm heterogeneity in S content in the mantle source (Fig. 8). We consider these differences reasonable based on the variation in S (Fig. 8a-c) and REE systematics in the chromite-hosted melt inclusions measured from the CLGB komatiites, which collectively suggest complex melting regime in the mantle source (Hanski and Kamenetsky 2013).

In all parental melts, the precipitated sulfide phase would become increasingly Cu-rich relative to Fe and Ni when the residual silicate melt crystallizes due to the compatibility of

Fe and Ni to the co-crystallizing olivine and Cr-spinel. In this case, the IPGE/PPGE of the precipitating equilibrium sulfide melt, regardless of its Ni/Cu, is initially controlled by the IPGE/PPGE of the silicate melt at sulfide saturation. Similar to sulfide melt fractionation, Cr-spinel is known to fractionate IPGE from PPGE, the former group showing stronger affinity to Cr-spinel (e.g., Pagé et al. 2012). In our simulations, Cr-spinel starts to crystallize ca. 100–200 °C before sulfide saturation, which is compatible with Re-Os data of natural Cr-spinel from Sakatti (Moilanen et al. 2021). This Cr-spinel fractionation should lead to gradually decreasing IPGE/PPGE in the residual silicate melt, which in turn should be reflected in the composition of the precipitating sulfide phase. The expected result is positive correlation between Ni/Cu and IPGE/PPGE as in the case of fractional crystallization of sulfide melt. We emphasize that these processes are not mutually exclusive, and it is likely that both can cause variability in sulfide compositions within a single magmatic system. Another important observation is that Cr-spinel crystallization precedes and continues during sulfide saturation, which implies that Ni and PGE contents of Cr-spinel could be a suitable sulfide exploration method (see e.g., Locmelis et al. 2018) in the context of CLGB komatiites. In addition, the simulated equilibrium sulfide compositions can help to determine if the natural sulfides are in equilibrium with their host rock.

Nickel content in olivine

Sulfide saturation state of olivine-saturated magmas can theoretically be inferred based on the Ni content of olivine, which can be used to guide sulfide deposit exploration (e.g., Naldrett et al. 1984; Naldrett 2004; Barnes et al. 2023b). However, without a proper baseline for Ni content in olivine formed during closed-system fractional crystallization, it is difficult to deduce if the host magma of olivine was sulfide saturated or not. Our simulations provide an estimate for the range of Ni content in olivine formed from sulfide-undersaturated CLGB komatiites. The olivine data from Kevitsa intrusion (Yang et al. 2013; Luolavirta et al. 2018a) and dyke (Nicklas et al. 2019; Puchtel et al. 2020) as well as Sakatti (Brownscombe et al. 2015; Höytiä unpublished) shows that the Ni contents are highly variable at constant MgO content (Fig. 6). The reason for the variable Ni contents in the most primitive olivine ($Fo_{93–94}$) is currently not known as discussed above. However, even this variability is not able to account for the even larger positive and negative deviations of the measured Ni contents compared to the simulated compositions at lower MgO contents (Fig. 6a, c–d). It is most likely that olivine with low Ni contents compared to our simulated olivine compositions formed from a sulfide-saturated melt. We suggest that the natural olivine populations from Kevitsa intrusion and Sakatti with relatively high Ni contents formed due to differing degrees of orthopyroxene fractionation in the lower crust (Fig. 6b). Transportation of orthopyroxene autocrysts from the depth could explain why the Kevitsa and Sakatti cumulates contain orthopyroxene (Brownscombe et al. 2015; Luolavirta et al. 2018a), which is not stable in the komatiitic melt at low pressure based on our simulations. We acknowledge that orthopyroxene could also form due assimilation of crustal rocks, especially in the thoroughly contaminated Kevitsa intrusion, and detailed mineral chemical study would be required to infer the origin of orthopyroxene.

Alternative processes that could explain the highest Ni contents of the Kevitsa and Sakatti olivine include minor pyroxenite component in the mantle source (e.g. Sobolev et al. 2007) or equilibration with Ni-rich sulfide melt (e.g., Barnes et al. 2023b). Presence of variable amounts of pyroxenite in the mantle source of the CLGB komatiites has been considered possible based on the REE characteristics (Hanski and Kamenetsky 2013). In addition to high Ni content, melt contribution from partly pyroxenitic mantle source should also lead to relatively high Fe/Mn (weight ratio typically > 75) in olivine (e.g., Sobolev et al. 2007; Gleeson and Gibson 2019). Considering those CLGB olivine in our database with Ni content > 3000 ppm ($n = 284$), the average Fe/Mn is 64 while only 14 grains have Fe/Mn > 75. Hence, we consider unlikely that pyroxenite component in the mantle source is the main cause of the variability in high Ni content of olivine in Kevitsa and Sakatti. We consider it possible that in dynamic magmatic systems such as Kevitsa and Sakatti (Brownscombe et al. 2015; Luolavirta et al. 2018a), near liquidus magma could have encountered pre-existing Ni-rich sulfides, and consequently the primitive olivine grains could have attained higher Ni content (see Barnes et al. 2023b for details). Indeed, this process has been suggested for the anomalous olivine in Kevitsa intrusion with 10,000–15,000 ppm Ni (Yang et al. 2013; Barnes et al. 2023b). For most of the olivine grains in our database, there is no documented spatial association with Ni-rich sulfides (Brownscombe et al. 2015; Luolavirta et al. 2018a; Höytiä unpublished), which makes it unlikely that the high Ni contents resulted from equilibration with sulfides. Moreover, Kevitsa and Sakatti contain mainly sulfides with low Ni/Cu, which should rather lead to sulfide melt scavenging Ni from the new magma pulse. Lastly, we expect that equilibration with sulfide melt should lead to MgO vs. Ni variation that is somewhat chaotic due to local variations in the relative amounts and compositions of sulfide and olivine. The observed MgO vs. Ni variation in the CLGB olivine is rather systematic and well-compatible with closed-system fractionation with variable degrees of early orthopyroxene crystallization (Fig. 6b).

Unfortunately, the effect of orthopyroxene fractionation increases the level of uncertainty when interpreting whether olivine formed from a sulfide-saturated magma. Whereas it is highly likely that olivine with lower Ni content compared to the estimate of our one-stage simulation (e.g. < 1000 ppm Ni; Fig. 6a–c) formed from sulfide-saturated magma, olivine with Ni-content between the compositions produced in the one and two-stage simulation are more ambiguous (e.g. between 1000 and 2000 ppm Ni; Fig. 6a–c). Some proxy could be used to identify if olivine formed from a melt that crystallized orthopyroxene + Cr-spinel in the lower crust to make better predictions of the expected Ni-content in olivine. One possibility could be Cr, which is a main component in Cr-spinel, compatible to orthopyroxene (Bédard 2007), and only moderately incompatible to olivine (Bédard 2005) at relevant conditions. Accordingly, lower crustal fractionation should lead to depletion of Cr in near-liquidus olivine with high MgO content. Indeed, olivine from Kevitsa intrusion (Yang et al. 2013; Luolavirta et al. 2018a) and Sakatti (Brownscombe et al. 2015; Höytiä unpublished) have generally $Cr_2O_3 \leq 0.1$ wt% (Table S3), whereas olivine in Kevitsa dyke contains 0.08–0.32 wt% Cr_2O_3 (Table S3) with an average of 0.17 wt% (Nicklas et al. 2019; Puchtel et al. 2020).

Finally, we acknowledge that other processes such as re-equilibration with interstitial residual silicate melt (see Barnes et al. 2023b) or new magma pulses (see Gleeson and Gibson 2019) have likely affected olivine compositions in Kevitsa intrusion and Sakatti. These processes tend to form olivine with higher Ni/Fo compared to fractional crystallization. However, neither of the re-equilibration processes can form olivine with higher Ni or Fo compared to the most primitive olivine. Olivine re-equilibration by either process is strongly dependent on the cooling history of the host rock and hence generally more extensive in long-lived magmatic systems (e.g., large intrusions or major magma pathways) compared to small sills or lava flows. Both Kevitsa and Sakatti were probably long-lived dynamic systems (Brownscombe et al. 2015; Luolavirta et al. 2018a), hence many of the olivine grains with higher Ni content compared to the simulated olivine composition may have formed due to some form of re-equilibration. While this process cannot form Ni-depleted olivine, it obscures identifying the proper baseline (via fractional crystallization) for Ni content in olivine based on the natural compositions only. For this reason, it is essential to identify the most primitive olivine of the magmatic system (i.e., olivine that is least re-equilibrated) to simulate the Ni content in olivine.

Conclusions

Our simulations provide a consistent petrogenetic model for the CLGB komatiites from the mantle source to the stage where they reach sulfide saturation at the crustal level. Based on the most primitive olivine populations in CLGB komatiites in Kevitsa and Sakatti, the parental melts had variable MgO contents in the range of 20.6–25.7 wt%. The simulation results suggest that the parental melts of the CLGB komatiites formed by various degrees of melting of a thermally heterogeneous (T_P = 1575–1700 °C) mantle source. Together with the PGE contents of the CLGB komatiites, the mantle melting simulations suggest complete dissolution of the mantle sulfide. The degrees of melting, however, remained low (< 22%), whereby the komatiites attained close to maximum S, Cu, and PPGE concentrations from the mantle source. Consequently, the komatiitic parental melts were almost as close to sulfide saturation as possible upon eruption or intrusion, which indicates that minimal S assimilation could have caused sulfide saturation. On the scale of CLGB, fractional crystallization was the dominant process controlling the liquid line of descent of the komatiites and hence the S solubility in the residual melt. Closed-system fractionation could have precipitated either Ni- or Cu-dominant sulfides depending on minor local differences in the degree of mantle melting or S content in the mantle source. The simulated Ni content in olivine is compatible with the natural data and provides a baseline to identify olivine grains from the CLGB komatiites and associated intrusive rocks that formed from Ni-depleted, hence likely sulfide-saturated, melt. For future, development of computational thermodynamic methods applicable to deep mantle conditions and inclusion of sulfide phase equilibrium to the thermodynamic simulations would greatly improve the quality of simulations related to ore critical systems and planetary S cycle in general.

Supplementary Information The online version contains supplementary material available at https://doi.org/10.1007/s00410-024-02154-9.

Acknowledgements We are grateful to Anglo American/AA Sakatti mining Oy and Pertti Lamberg for the permit to publish the olivine data, and to Max Renlund and Mia Tiljander for conducting the unpublished Sakatti olivine measurements. We thank Eric Brown for instructions related to REEBOX PRO, and Fabrice Gaillard, Ken Koga, Hugh O'Neill, and Christoph Beier for discussions related to mantle melting. We are thankful for the thorough and constructive comments from the editor Dante Canil, and reviewers Igor S. Puchtel and Pedro Waterton.

Funding Open Access funding provided by University of Helsinki (including Helsinki University Central Hospital). This study is supported by the SEMACRET project (101057741) co-funded by Horizon Europe program and UK Research Innovation. H.M.A.H. is funded by a personal research grant from K.H. Renlund Foundation.

Competing interests Author H.M.A.H. is an employee at the Anglo American/AA Sakatti Mining Oy that is the owner of the Sakatti Cu-Ni-PGE project. Otherwise, the authors have no relevant financial or non-financial interests to disclose.

References

Arndt NT (1977) Partitioning of nickel between olivine and ultrabasic and basic komatiite liquids. Carnegie Inst Wash Yearbook 76:553–557

Arndt N, Lesher CM, Czamanske GK (2005) Mantle-derived magmas and magmatic Ni-Cu-(PGE) deposits. In: Hedenqvist JW, Thompson JFH, Goldfarb RJ, Richards JP (eds.) Economic Geology One Hundreth Anniversary Volume, Society of Economic Geologists, Ottawa, pp. 5–24. https://doi.org/10.5382/AV100.02

Arndt N, Lesher CM, Barnes SJ (2008) Komatiite. Cambridge University Press, New York. https://doi.org/10.1017/CBO9780511535550

Barnes S-J, Lightfoot PC (2005) Formation of magmatic nickel sulfide ore deposits and processes affecting their copper and platinum group element contents. In: Hedenqvist JW, Thompson JFH, Goldfarb RJ, Richards JP (eds.) Economic Geology One Hundreth Anniversary Volume, Society of Economic Geologists, Ottawa, pp. 179–213. https://doi.org/10.5382/AV100.08

Barnes S-J, Often M (1990) Ti-rich komatiites from northern Norway. Contrib Mineral Petrol 105:42–54. https://doi.org/10.1007/BF00320965

Barnes SJ, Cruden AR, Arndt N, Saumur BM (2016) The mineral system approach applied to magmatic Ni-Cu-PGE sulphide deposits. Ore Geol Rev 76:296–316. https://doi.org/10.1016/j.oregeorev.2015.06.012

Barnes S-J, Mansur ET, Maier WD, Prevec SA (2023a) A comparison of trace element concentrations in chromites from komatiites, picrites, and layered intrusions: implications for the formation of massive chromite layers. Can J Earth Sci 60:97–132. https://doi.org/10.1139/cjes-2022-0064

Barnes SJ, Yao Z-S, Mao Y-J, Jesus AP, Yang S, Taranovic V, Maier WD (2023b) Nickel in olivine as an exploration indicator for magmatic Ni-Cu deposits: a data review and re-evaluation. Am Min 108:1–17. https://doi.org/10.2138/am-2022-8327

Bédard JH (2005) Partition coefficients between olivine and silicate melts. Lithos 83:394–419. https://doi.org/10.1016/j.lithos.2005.03.011

Bédard JH (2006) Trace element partitioning in plagioclase feldspar. Geochim Cosmochim Acta 70:3717–3742. https://doi.org/10.1016/j.gca.2006.05.003

Bédard JH (2007) Trace element partitioning coefficients between silicate melts and orthopyroxene: parameterizations of D variations. Chem Geol 244:263–303. https://doi.org/10.1016/j.chemgeo.2007.06.019

Bédard JH (2014) Parameterizations of calcic clinopyroxene–melt trace element partition coefficients. Geochem Geophys Geosyst 15:303–336. https://doi.org/10.1002/2013GC005112

Bekker A, Barley ME, Fiorentini ML, Rouxel OJ, Rumble D, Beresh-ford SW (2009) Atmospheric sulfur in Archean komatiite-hosted nickel deposits. Science 326:1086–1089. https://doi.org/10.1126/science.1177742

Bohrson WA, Spera FJ, Ghiorso MS, Brown GA, Creamer JB, Mayfield A (2014) Thermodynamic model for energy-constrained open-system evolution of crustal magma bodies undergoing simultaneous recharge, assimilation and crystallization: the Magma chamber simulator. J Petrol 55:1685–1717. https://doi.org/10.1093/petrology/egu036

Brown EL, Lesher CE (2016) REEBOX PRO: a forward model simulating melting of thermally and lithologically variable upwelling mantle. Geochem Geophys Geosyst 17:3929–3968. https://doi.org/10.1002/2016GC006579

Brownscombe W, Ihlenfeld C, Coppard J, Hartshorne C, Klatt S, Siikaluoma JK, Herrington RJ (2015) The Sakatti Cu-Ni-PGE sulfide depositin northern Finland. In: Maier WD, Lahtinen R, O'Brien H (eds) Mineral deposits of Finland. Elsevier, Amsterdam, pp 211–252. https://doi.org/10.1016/B978-0-12-410438-9.00009-1

Deschamps F, Godard M, Guillot S, Hattori K (2013) Geochemistry of subduction zone serpentinites: a review. Lithos 178:96–127. https://doi.org/10.1016/j.lithos.2013.05.019

Fortin M-A, Riddle J, Desjardins-Langlais Y, Baker DR (2015) The effect of water of the sulfide concentration at sulfide saturation (SCSS) natural melts. Geochim Cosmochim Acta 160:100–116. https://doi.org/10.1016/j.gca.2015.03.022

Fröhlich F, Siikaluoma J, Osbahr I, Gutzmer J (2021) Genesis of sulfide vein mineralization in the Sakatti Ni-Cu-PGE deposit, Finland. Canad Mineral 59:1485–1510. https://doi.org/10.3749/canmin.2100020

Gangopadhyay A, Walker RJ, Hanski E, Solheid PA (2006) Origin of Paleoproterozoic komatiites at Jeesiörova, Kittilä Greenstone Belt Complex, Finnish Lapland. J Petrol 47:773–789. https://doi.org/10.1093/petrology/egi093

Ghiorso MS, Gualda GAR (2015) An H2O-CO2 mixed fluid saturation model compatible with rhyolite-MELTS. Contrib Mineral Petrol 169:1–30. https://doi.org/10.1007/s00410-015-1141-8

Ghiorso MS, Sack RO (1995) Chemical mass transfer in magmatic processes. IV. A revised and internally consistent thermodynamic model for the interpolation and extrapolation of liquid-solid equilibria in magmatic systems at elevated temperatures and pressures. Contrib Mineral Petrol 119:197–212. https://doi.org/10.1007/BF00307281

Ghiorso MS, Hirschmann MM, Reiners PW, Kress VC III (2002) The pMELTS: a revision of MELTS for improved calculation of phase relations and major element partitioning related to partial melting of the mantle to 3 GPa. Geochem Geophys Geosyst 3:1–35. https://doi.org/10.1029/2001GC000217

Gleeson MLM, Gibson SA (2019) Crustal controls on apparent mantle pyroxenite signals in ocean-island basalts. Geology 47:321–324. https://doi.org/10.1130/G45759.1

Green DH, FalloonTJ (1998) Pyrolite: a Ringwood concept and its current expression. In: Jackson INS (ed) The Earth's Mantle: composition, structure, and evolution. Cambridge University Press, Cambridge, pp 311–378

Hansen H, Slagstad T, Bergh SG, Bekker A (2023) Geochronology and chemostratigraphy of the 2.47–1.96 Ga rift-related volcano-sedimentary succession in the Karasjok Greenstone Belt, northern Norway, and its regional correlation within the Fennoscandian Shield. Precambrian Res 397:1–24. https://doi.org/10.1016/j.precamres.2023.107166

Hanski E, Huhma H (2005) Central Lapland greenstone belt. In: Lehtinen M, Nurmi PA, Rämö OT (eds) Precambrian geology of Finland–key to the evolution of the Fennoscandian Shield. Elsevier, Amsterdam, pp 139–193. https://doi.org/10.1016/S0166-2635(05)80005-2

Hanski E, Kamenetsky VS (2013) Chrome spinel-hosted melt inclusions in Paleoproterozoic primitive volcanic rocks, northern Finland: evidence for coexistence and mixing of komatiitic and picritic magmas. Chem Geol 343:25–37. https://doi.org/10.1016/j.chemgeo.2013.02.009

Hanski E, Huhma H, Rastas P, Kamenetsky VS (2001) The paleoproterozoic komatiite-picrite association of Finnish Lapland. J Petrol 42:855–876. https://doi.org/10.1093/petrology/42.5.855

Haverinen J (2020) Evaporites in the Central Lapland Greenstone Belt. Master's thesis, University of Helsinki. http://hdl.handle.net/10138/324285

Heinonen JS, Bohrson WA, Spera FJ, Brown GA, Scruggs MA, Adams JV (2020) Diagnosing open-system magmatic processes using the Magma Chamber Simulator (MCS): part II—trace elements and isotopes. Contrib Mineral Petrol 175:1–21. https://doi.org/10.1007/s00410-020-01718-9

Herzberg C (2022) Understanding the Paleoproterozoic Circum-Superior large Igneous Province constrains the thermal properties of Earth's mantle through time. Precambrian Res 375:1–17. https://doi.org/10.1016/j.precamres.2022.106671

Herzberg C, Asimow PD, Arndt N, Niu Y, Lesher CM, Fitton JG, Cheadle MJ, Saunders AD (2007) Temperatures in ambient mantle and plumes: constraints from basalts, picrites, and komatiites. Geochem Geophys Geosyst 8:1–34. https://doi.org/10.1029/2006GC001390

Hirschmann MM, Ghiorso MS, Wasylenki LE, Asimow PD, Stolper EM (1998) Calculation of Peridotite partial melting from Thermodynamic Models of Minerals and melts. I. Review of methods and comparison with experiments. J Petrol 39:1091–1115. https://doi.org/10.1093/petroj/39.6.1091

Holness MB (2000) Metasomatism and self-organization of dolerite dyke-marble contacts: Beinn an Dubhaich, Skye. J Metamorphic Geol 18:103–118. https://doi.org/10.1046/j.1525-1314.2000.00244.x

Hölttä P, Heilimo E (2017) Metamorphic map of Finland. Geological survey of Finland. Special Paper 60:77–128

Huhma H, Hanski E, Kontinen A, Vuollo J, Mänttäri I, Lahaye Y (2018) Sm-Nd and U-Pb isotope geochemistry of the Palaeoproterozoic mafic magmatism in eastern and northern Finland. Geol Surv Finland Bull 405:1–150

Keays RR (1995) The role of komatiitic and picritic magmatism and S-saturation in the formation of ore deposits. Lithos 34:1–18. https://doi.org/10.1016/0024-4937(95)90003-9

Kiseeva ES, Wood BJ (2015) The effects of composition and temperature on chalcophile and lithophile element partitioning into magmatic sulphides. Earth Planet Sci Lett 424:280–294. https://doi.org/10.1016/j.epsl.2015.05.012

Korenaga J (2008) Plate tectonics, flood basalts and the evolution of Earth's oceans. Terra Nova 20:419–439. https://doi.org/10.1111/j.1365-3121.2008.00843.x

Kovalenko VI, Naumov VB, Girnis AV, Dorofeeva VA, Yarmolyuk VV (2007) Average compositions of magmas and mantle sources of mid- ocean ridges and intraplate oceanic and continental settings estimated from the data on melt inclusions and quenched glasses of basalts. Petrology 15:361–396. https://doi.org/10.1134/S0869591107040029

Köykkä J, Lahtinen R, Huhma H (2019) Provenance evolution of the Paleoproterozoic metasedimentary cover sequences in northern Fennoscandia: Age distribution, geochemistry, and zircon morphology. Precambrian Res 331:1–21. https://doi.org/10.1016/j.precamres.2019.105364

Lahtinen R, Korja A, Nironen M (2005) Paleoproterozoic tectonic evolution. In: Lehtinen M, Nurmi PA, Rämö OT (eds) Precambrian geology of Finland–key to the evolution of the Fennoscandian Shield. Elsevier, Amsterdam, pp 481–531. https://doi.org/10.1016/S0166-2635(05)80012-X

Le Vaillant M, Barnes SJ, Fiorentini ML, Santaguida F, Törmänen T (2016) Effect of hydrous alteration on the distribution of base metals and platinum group elements within the Kevitsa magmatic nickel sulfide deposit. Ore Geol Rev 72:128–148. https://doi.org/10.1016/j.oregeorev.2015.06.002

Lesher CM, Burnham OM (2001) Multicomponent elemental and isotopic mixing in Ni-Cu-(PGE) ores at Kambalda, Western Australia. Canad Mineral 39:421–446. https://doi.org/10.2113/gscanmin.39.2.421

Li C, Maier WD, de Waal SA (2001) Magmatic Ni-Cu versus PGE deposits: contrasting genetic controls and exploration implications. S Afr J Geol 104:309–318. https://doi.org/10.2113/gssajg.104.4.309

Liu J, Xia QK, Kuritani T, Hanski E, Yu H-R (2017) Mantle hydration and the role of water in the generation of large igneous provinces. Nat Commun 8:1–8. https://doi.org/10.1038/s41467-017-01940-3

Locmelis M, Fiorentini ML, Barnes SJ, Hanski EJ, Kobussen AF (2018) Ruthenium in chromite as indicator for magmatic sulfide liquid equilibration in mafic-ultramafic systems. Ore Geol Rev 97:152–170. https://doi.org/10.1016/j.oregeorev.2018.05.002

Lorand J-P, Luquet A (2016) Chalcophile and siderophile elements in mantle rocks: trace elements controlled by trace minerals. In: Harvey J, Day J (eds) Highly Siderophile and strongly Chalcophile Elements in High-Temperature Geochemistry and Cosmochemistry, Reviews in Mineralogy and Petrology 81. The Mineralogical Society of America, Virginia, pp 441–488. https://doi.org/10.1515/9781501502095-010

Luolavirta K, Hanski E, Maier W, Santaguida F (2018a) Characterization and origin of dunitic rocks in the Ni-Cu-(PGE) sulfide ore-bearing Kevitsa intrusion, northern Finland: whole-rock and mineral chemical constraints. Bull Geol Soc Finland 90:5–32. https://doi.org/10.17741/bgsf/90.1.001

Luolavirta K, Hanski E, Maier W, Santaguida F (2018b) Whole-rock and mineral compositional constraints on the magmatic evolution of the Ni-Cu-(PGE) sulfide ore-bearing Kevitsa intrusion, northern Finland. Lithos 296–299:37–53. https://doi.org/10.1016/j.lithos.2017.10.015

Luukas J, Kousa J, Nironen M, Vuollo J (2017) Major stratigraphic units in the bedrock of Finland, and an approach to tectonostratigraphic division. Geological Survey of Finland, Special Paper 60:9–40

Malvoisin B (2015) Mass transfer in the oceanic lithosphere: serpentinization is not isochemical. Earth Planet Sci Lett 430:75–85. https://doi.org/10.1016/j.epsl.2015.07.043

Matzen AK, Baker MB, Beckett JR, Stolper EM (2011) Fe-Mg partitioning between Olivine and High-magnesian melts and the nature of hawaiian parental liquids. J Petrol 52:1243–1263. https://doi.org/10.1093/petrology/egq089

Matzen AK, Baker MB, Beckett JR, Stolper EM (2013) The temperature and pressure dependence of nickel partitioning between olivine and silicate melt. J Petrol 54:2521–2545. https://doi.org/10.1093/petrology/egt055

Matzen AK, Baker MB, Beckett JR, Wood BJ, Stolper EM (2017) The effect of liquid composition on the partitioning of ni between olivine and silicate melt. Contrib Mineral Petrol 172:1–18. https://doi.org/10.1007/s00410-016-1319-8

Miller GH, Stolper EM, Ahrens TJ (1991) The equation of state of a molten komatiite 2. Application to komatiite petrogenesis and the Hadean mantle. J Geophys Res 96:11849–11864. https://doi.org/10.1029/91JB01203

Moilanen M, Hanski E, Yang S-H (2021) Re-os isotope geochemistry of the Paleoproterozoic Sakatti Ci-Ni-PGE sulphide deposit in northern Finland. Ore Geol Rev 132:1–16. https://doi.org/10.1016/j.oregeorev.2021.104044

Mungall JE (2014) Geochemistry of magmatic ore deposits. In: Holland HD, Turekian KK (eds) Treatise on Geochemistry, 2nd edn. Elsevier, Amsterdam, pp 195–218. https://doi.org/10.1016/B978-0-08-095975-7.01108-6

Mutanen T (1997) Geology and ore petrology of the Akanvaara and Koitelainen mafic layered intrusions and the Keivitsa-Satovaara layered complex, northern Finland. Geol Surv Finland Bull 395:1–233

Mutanen T, Huhma H (2001) U-Pb geochronology of the Koitelainen, Akanvaara and Keivitsa mafic layered intrusions and related rocks. In: Vaasjoki M (ed), Radiometric age determinations from Finnish Lapland and their bearing on the timing of Precambrian volcano-sedimentary sequences. Geol Surv Finl, Spec Pap 33:229–246

Naldrett AJ (2004) Magmatic sulfide deposits: geology, geochemistry and exploration. Springer, Berlin

Naldrett AJ, Duke JM, Lightfoot PC, Thompson JFH (1984) Quantitative modelling of the segregation of magmatic sulphides: an exploration guide. CIM Bull 77:1–10

Nicklas RW, Puchtel IS, Ash RD, Piccoli PM, Hanski E, Nisbet EG, Waterton P, Pearson DG, Anbar AD (2019) Secular mantle oxidation across Archean-Proterozoic boundary: evidence from V partitioning in komatiites and picrites. Geochim Cosmochim Acta 250:49–75. https://doi.org/10.1016/j.gca.2019.01.037

Nicklas RW, Puchtel IS, Baxter EF (2024) Concordance of V-in-olivine and Fe-XANES oxybarometry methods in mid-ocean ridge basalts. Earth Planet Sci Lett 625:1–8. https://doi.org/10.1016/j.epsl.2023.118492

O'Neill HStC (2021) The thermodynamic controls on sulfide saturation in silicate melts with application to ocean floor basalts. In: Moretti R, Neuville DR (eds) Magma Redox chemistry, 1st edn. Wiley, New Jersey, pp 177–213. https://doi.org/10.1002/9781119473206.ch10

Orvik AA, Slagstad T, Hansen H, Nilsson LP, Sørensen BE (2022) The Palaeoproterozoic Gallujavri ultramafic intrusion, Karasjok Greenstone Belt; petrogenesis of a trans-crustal magma system. J Petrol 63:1–28. https://doi.org/10.1093/petrology/egac008

Pagé P, Barnes S-J, Bédard JH, Zientek ML (2012) In situ determination of os, ir, and Ru in chromites formed from komatiite, tholeiite and boninite magmas: implications for chromite control of os, ir and Ru during partial melting and crystal fractionation. Chem Geol 302–303:3–15. https://doi.org/10.1016/j.chemgeo.2011.06.006

Papunen H (1998) Geology and ultramafic rocks of the Paleoproterozoic Pulju Greenstone Belt, western Lapland. Geological Survey of Finland, Technical Report 6.5:1–57

Patten CGC, Molnár F, Pitcairn IK, Kolb J, Mertanen S, Hector S (2023) Multi-source and multi-stage metal mobilization during the tectonic evolution of the Central Lapland Greenstone Belt, Finland: implications for the formation of orogenic au deposits. Min Deposita 58:461–488. https://doi.org/10.1007/s00126-022-01133-z

Pouchou JL, Pichoir F (1986) Basic expression of PAP computation for quantitative EPMA. In: Brown JD, Packwood RH (eds.) 11th international Congress on X-ray Optics and Microanalysis (ICXOM), 249–253

Puchtel IS, Mundl-Petermeier A, Horan M, Hanski EJ, Blichert-Toft J, Walker RJ (2020) Ultra-depleted 2.05 Ga komatiites of Finnish Lapland: products of grainy late accretion of core-mantle interaction? Chem Geol 554:1–23. https://doi.org/10.1016/j.chemgeo.2020.119801

Räsänen J (2008) Keski-Lapin liuskevyöhykkeen geologinen kehitys Sodankylän liuskealueella. Geological Survey of Finland, Archive Report K21.42/2008/25:1–18

Rasilainen K, Lahtinen R, Bornhorst TJ (2007) The rock geochemical database of Finland: manual. Geological survey of Finland. Rep Invest 164:1–38

Santaguida F, Luolavirta K, Lappalainen M, Ylinen J, Voipio T, Jones S (2015) The Kevitsa Ni-Cu-PGE deposit in the Central Lapland Greenstone Belt in Finland. In: Maier WD, Lahtinen R, O'Brien H (eds) Mineral deposits of Finland. Elsevier, Amsterdam, pp 195–210. https://doi.org/10.1016/B978-0-12-410438-9.00008-X

Saverikko M (1985) The pyroclastic komatiite complex at Sattasvaara in northern Finland. Bull Geol Soc Finland 57:55–87. https://doi.org/10.17741/bgsf/57.1-2.005

Sayab M, Lahtinen R, Köykkä J, Hölttä P, Karinen T, Niiranen T, Leväniemi H (2021) Improved resolution of Paleoproterozoic orogenesis: multi-directional collision tectonics in the Sodankylä belt of northern Finland. Precambrian Res 359:1–23. https://doi.org/10.1016/j.precamres.2021.106193

Smythe DJ, Wood BJ, Kiseeva ES (2017) The S content of silicate melts at sulfide saturation: new experiments and a model incorporating the effects of sulfide composition. Am Min 102:795–803. https://doi.org/10.2138/am-2017-5800CCBY

Sobolev AV, Hofmann AW, Kuzmin DV, Yaxley GM, Arndt NT, Chung S-L, Danyushevsky LV, Elliott T, Frey FA, Garcia MO, Gurenko AA, Kamenetsky VS, Kerr AC, Krivolutskaya NA, Matvienkov VV, Nikogosian IK, Rocholl A, Sigurdsson IA, Sushchevskaya NM, Teklay M (2007) The amount of recycled crust in sources of mantle-derived melts. Science 316:412–417. https://doi.org/10.1126/science.1138113

Sossi PA, O'Neill HStC (2016) Liquidus temperatures of komatiites and the effect of cooling rate on element partitioning between olivine and komatiitic melt. Contrib Mineral Petrol 171:1–25. https://doi.org/10.1007/s00410-016-1260-x

Sossi PA, Eggins SM, Nesbitt RW, Nebel O, Hergt JM, Campbell IH, Van O'Neill HStC M, Davies DR (2016) Petrogenesis and geochemistry of Archean komatiites. J Petrol 57:147–184. https://doi.org/10.1093/petrology/egw004

Sun Z, Xiong X, Wang J, Liu X, Li L, Ruan M, Zhang L, Takahashi E (2020) Sulfur abundance and heterogeneity in the MORB mantle estimated by copper partitioning and sulfur solubility modeling. Earth Planet Sci Lett 538:1–11. https://doi.org/10.1016/j.epsl.2020.116169

Törmänen T, Konnunaho JP, Hanski E, Moilanen M, Heikura P (2016) The paleoproterozoic komatiite-hosted PGE mineralization at Lomalampi, Central Lapland Greenstone Belt, northern Finland. Min Deposita 51:411–430. https://doi.org/10.1007/s00126-015-0615-y

Walter MJ (1998) Melting of garnet peridotite and the origin of komatiite and depleted lithosphere. J Petrol 39:29–60. https://doi.org/10.1093/petroj/39.1.29

Waterton P, Pearson DG, Mertzman SA, Mertzman KR, Kjarsgaard BA (2020) A FractionalCrystallization link between komatiites, basalts, and dunites of the Palaeoproterozoic Winnipegosis Komatiite Belt, Manitoba, Canada. J Petrol 61:1–34. https://doi.org/10.1093/petrology/egaa052

Waterton P, Mungall J, Pearson DG (2021) The komatiite-mantle platinum-group element paradox. Geochim Cosmochim Acta 313:214–242. https://doi.org/10.1016/j.gca.2021.07.037

Workmann RK, Hart SR (2005) Major and trace element composition of the depleted MORB mantle (DMM). Earth Planet Sci Lett 231:53–72. https://doi.org/10.1016/j.epsl.2004.12.005

Yang S-H, Maier WD, Hanski EJ, Lappalainen M, Santaguida F, Määttä S (2013) Origin of ultra-nickeliferous olivine in the Kevitsa Ni-Cu-PGE-mineralized intrusion, northern Finland.

Contrib Mineral Petrol 166:81–95. https://doi.org/10.1007/s00410-013-0866-5

Yao Z, Qin K, Mungall JE (2018) Tectonic controls on Ni and Cu contents of primary mantle-derived magmas for the formation of magmatic sulfide deposits. Am Min 103:1545–1567. https://doi.org/10.2138/am-2018-6392